ORNL/TM-2018/1044
Final Report for CRADA/NFE-16-06224

Fluid Dynamics Effects on Microstructure Prediction in Single Laser Tracks for Additive Manufacturing

Adrian S. Sabau
Lang Yuan
Narendran Raghavan
Srdjan Simunovic
John Turner
Vipul K. Gupta

October 2018

OAK RIDGE NATIONAL LABORATORY
MANAGED BY UT-BATTELLE FOR THE US DEPARTMENT OF ENERGY

ORNL/TM-2018/1044
Final Report for CRADA/NFE-16-06224

High-Performance Computing for Manufacturing Project Program (HPC4Mfg)

Fluid Dynamics Effects on Microstructure Prediction in Single Laser Tracks for Additive Manufacturing

Adrian S. Sabau
Lang Yuan
Narendran Raghavan
Srdjan Simunovic
John Turner
Vipul K. Gupta

October 2018

Prepared by
OAK RIDGE NATIONAL LABORATORY
Oak Ridge, TN 37831-6283
managed by
UT-BATTELLE, LLC
for the
US DEPARTMENT OF ENERGY
under contract DE-AC05-00OR22725

CONTENTS

Page

LIST OF FIGURES

LIST OF TABLES

ACKNOWLEDGEMENTS

This research was conducted for the project "Process Maps for Tailoring Microstructure in Laser Powder-Bed Fusion Additive Manufacturing" and was supported by the High-Performance Computing for Manufacturing Project Program (HPC4Mfg), managed by the U.S. Department of Energy Advanced Manufacturing Office within the Energy Efficiency and Renewable Energy Office. It was performed under the auspices of the US Department of Energy by Oak Ridge National Laboratory under contract No. DE-AC0500OR22725, UT-Battelle, LLC. in collaboration with GE Global Research (GEGR). The authors would like to thank:

- Matt Bement of Los Alamos National Laboratory, for the initial Truchas installation, maintenance, and run scripts on Titan,
- Neil Carlson of Los Alamos National Laboratory, Truchas developer project leader, for feedback during the project.

ABSTRACT

The Laser Powder Bed Fusion Additive Manufacturing (LPBFAM) is one of the most important processes for the production of lightweight, cost-effective, complex, and high-performance end-use parts. At present, the cost and time associated with LPBFAM process development is very high due to a lack of fundamental process understanding. In this project, a multi-physics model was developed on a highly parallel open-source code, Truchas, with the ultimate goal of providing experimentally validated process maps for tailoring microstructure to achieve desired performance for LPBFAM. As a critical step towards fully LPBFAM modeling, modeling of single-track laser fusion (STLF) were conducted. Multi-physics simulations were conducted using Truchas for STLF by considering heat transfer, phase-change, fluid dynamics, surface tension phenomena, and evaporation. In order to assess the effect of the fluid dynamics on the solidification and ensuing microstructure, a heat transfer-and-solidification-only (HTS) model and a fully coupled heat-transfer-solidification and fluid-dynamics (HTS-FD) model were considered. In the HTS_FD model, the fluid flow was considered to be laminar while the molten alloy surface is assumed to be flat and non-deformable. This study is one the first attempt to understand the effect of the fluid flow on microstructure in STLF and LPBFAM. The results show that the fluid flow affects the solidification and ensuing microstructure in STLF.

In order to validate Truchas for STLF and LPBFAM modeling, experimental data, which was obtained at GE Global Research (GEGR) for liquid pool shape and microstructure, were compared with those from numerical simulation results. For the keyhole regime case, numerical simulation results indicate that the melt-pool shape was typical to that of the conduction case with very large deviations from the measured melt-pool depths. Two sensitivity studies were conducted by varying the evaporation flux and the surface tension coefficient at fixed laser absorptivities of 0.5 and 0.3, respectively. The minimum value for the overall combined error, between the calculated values with the HTS_FD model and measured values for both the width and height of the melt-pool, was attained for a surface tension coefficient of -0.75e-4 N/m.

An analytical solidification model for the columnar-to-equiaxed transition (CET) in rapid solidification was used to assess the microstructure variation within the melt-pool. From numerical simulation results, thermal gradient, G, and solidification velocity, V, were obtained in order to predict the microstructure type (e.g., dendritic, cellular). For the fluid-flow HTS_FD model, G was found to exhibit a maximum at the extremity of the solidified pool (i.e., at the free surface). By contrast, for HTS simulations, G was found to exhibit a maximum around the entire edge of the solidified pool. For the HTS_FD simulations, the minimum values of the cooling rate, GV, were found to be approximately half than their corresponding values for HTS simulations. By contrast with the min GV values, the maximum values for GV were found to occur for the HTS_FD simulations. Thus, HTS_FD simulations were found to exhibit a wider range of cooling rates than the HTS simulations. Concerning the solidification maps, the variation of the solidification velocity, V, as function of the thermal gradient, G, was obtained. It was found that the fluid flow model results (HTS_FD) exhibited an increased spread in the V(G) variation within the melt pool with respect to the HTS model results (without the fluid flow).

A preliminary correlation model for the primary dendrite arm spacing (PDAS) based on a power law dependence on thermal gradient and solidification velocity was used to estimate PDAS from HTS and HTS_FD simulations. For low laser powers and low laser speeds, the PDAS obtained

with the fluid dynamics model (HTS_FD) was larger by more than 30% with respect to the PDAS calculated with the simple HTS model.

In the second part of the project, fifty-seven simulations were conducted in order to obtain data on microstructure variables that can be used for process map development. In order to cover the entire processing space, thirty-three cases were selected STLF process simulations at six power levels and six laser scanning speeds. The 57 STLF process simulations were conducted as follows: 33 simulations with the heat-transfer-only (HTS) model and 24 simulations with the fluid flow model (HTS_FD). The solidification map data shows that for all simulations, a columnar dendritic microstructure would be expected. It was found that the minimum, average, and maximum thermal gradient exhibit exponential variations with respect to a process variable defined as the ratio between the power and square root of scan speed.

Expected Benefits

The deployment of the new open-source software tool and process maps will have the potential to:

- Accelerate process certification as required by manufacturers.
- Accelerate new product introduction,
- Improve the fidelity of the physical models, establishing a science-based foundation for dealing with process challenges in LPBFAM,
- Decrease the CPU time for complex transient phenomena enough to impact design cycles and optimize process development, and
- Enable the straightforward adaptation to other related metal AM processes.

1. OBJECTIVES AND BACKGROUND

The main objective of this Cooperative Research and Development Agreement (CRADA) project between GE Global Research (GEGR) and ORNL was to investigate the development of a process map for the Laser Powder Bed Fusion Additive Manufacturing (LPBFAM) process based on multi-physics simulations that consider fluid flow effects. As a critical step towards fully LPBFAM modeling, modeling of single-track laser fusion (STLF) were conducted first. GEGR experts on both AM process and materials science worked closely with ORNL researchers to adapt Truchas for LPBFAM to: 1) develop process and solidification models, and 2) generate process maps for melt pool size and microstructure prediction.

The HPC4Mfg Program provides the perfect platform for GEGR to work with ORNL on the above challenges. GEGR's expertise in industrial application and experience with manufacturing processes brought the best industrial practice to the program. ORNL's expertise on advanced modeling and simulation and code development for LPBFAM was very important for this project. This collaboration with timely support from HPC4Mfg will aid in maturing the technology on process modeling to address the manufacturing challenges in optimizing of process parameters and tailoring microstructures for desired performance.

1.1 BACKGROUND

Additive Manufacturing (AM) is a revolutionary manufacturing process with clear advantages such as lower energy usage, minimum scrap waste, lower buy-to-fly ratio and shorter lead time to market. The LPBFAM process is one of the most important forms to realize lightweight and cost-effective production of complex, high-performance end-use parts. As a result, this technology is being deployed at an accelerated pace across the world. At present, the cost and time associated with LPBFAM process development for LPBFAM is very high due to a lack of fundamental process understanding. Furthermore, deployed processes are largely sub-optimal. This prevents the full exploration of the component design space to the realization of energy savings.

A large gap exists in the AM process development to link process parameters to microstructure and final part performance. The widespread and economical use of metal AM relies on the ability to predict and control microstructures and resulting mechanical properties. Process maps that link solidification conditions to melt-pool size and shape, and microstructure will significantly reduce process development time and accelerate process certification and new product introduction.

2. BENEFITS TO THE DOE AMO OFFICE'S MISSION

The work performed under this CRADA directly supported DOE's mission in the Advanced Manufacturing Office of the Office of Energy Efficiency and Renewable Energy by providing modeling and simulation data for Laser Powder Bed Fusion Additive Manufacturing (LPBFAM) process. The modeling tool developed in this project will be available to the industry in large, including automotive, aerospace, machinery, electronics, and medical, to transform their current trial-and-error based methodology to digital tool guided and physics-based methodology. This will not only help to compress time to explore large parameter space to achieve optimal microstructure, accelerating the development and deployment time of AM processes for desired performance, but also will open new possibilities for process development in identifying solutions outside of current process parameter space. The developed tools will enable inclusion of more physical phenomena in the models and perform calculations that capture transient phenomena quickly enough to impact design cycles, where HPC facilities become widely available, and thus reduce both cost and significant energy consumption on physical experiments. Process development is also a key part towards certification of LPBFAM materials and processes.

Significant benefits of AM have been reported by U.S. Department of Energy (DOE) (AMO, 2012). For instance, AM can reduce materials needs and cost by up to 90% and use only 2-25% of energy to remanufacturing parts to return end-of-life products to as-new condition. The manufacturing flexibility from AM also yields organic design with light weight, which will help on cutting CO_2 emissions for industry in general. Most recent data on energy and emissions saving potential of AM for aerospace industry showed that: with lightweight and cost-effective designs for aircraft components, estimated fleet-wide life-cycle primary energy savings at most reach 70-173 million GJ/year in 2050, with cumulative savings of 1.2–2.8 billion GJ. Associated cumulative CO_2 emission reductions were estimated at 92.1–215.0 million metric tons. In addition, thousands of tons of aluminum, titanium and nickel alloys could be potentially saved per year (Huang et al., 2015). The AM technology, which improves materials efficiency,

reduces life-cycle impacts, and enables greater engineering functionality, has been increasingly adopted by several industries (automotive, aerospace, machinery, electronics, and medical). A compound annual growth rate (CAGR) of 35.2% has been reported in 2014, the highest in two decades (Wohlers Associates, 2015). The adoption of AM is projected to increase from $365.4M in 2015 to $1.8B in 2023, attaining a 19.51% CAGR for automotive industry; from $723M in 2015 to $3.45B in 2023, an 18.97% CAGR for aerospace industry (Columbus, 2015).

3. TECHNICAL DISCUSSION OF WORK PERFORMED BY ALL PARTIES

While AM continues to expand dramatically, the cost and time associated with the process development for LPBFAM are still high and slow, respectively (Frazier, 2014). A large gap exists in the AM process development to link process parameters to microstructure and part performance. The widespread and economical use of metal AM relies on the ability to predict and control microstructures and resulting mechanical properties. Process maps that link solidification conditions to melt-pool size and microstructure will significantly reduce process development time and accelerate process certification and new product introduction.

Process maps for Laser Engineered Net Shaping (LENS) process were developed (Vasinonta et al., 1999; Vasinonta et al., 2001; and Beuth and Klingbeil, 2001). However, the extension to LPBFAM of those process maps is constrained by computational resources and consolidated solidification theory with insufficient validation data, due to much higher spatial and temporal resolution specific to LPBFAM. In LPBFAM, by varying particle size distribution (PSD) of powder, laser parameters (power, scan speed, beam diameter, and hatch spacing), metal alloys can experience large range of solidification conditions (Bontha et al., 2006), namely, temperature gradient (G) and solidification velocity (V), from ~1,000 K/m to 1,000,000 K/m and ~0 m/s to 10 m/s, respectively. The resulting solidification microstructure will vary dramatically based on the process parameters (Hunt, 1984). Current solutions to predict thermal history in LPBFAM is using either an analytical approach, e.g., Rosenthal solution (Bontha et al., 2006) or commercially available FEA software (Vasinonta et al., 2007). These computational resources and expertise available at ORNL are not available at GEGR and are crucial for addressing three main challenges listed below with the proposed solutions to advance the process development of LPBFAM:

A. Analytical approaches are the most efficient methods, but they lack accuracy as the solution is dominated by heat transfer without temperature-dependent material properties.
B. Finite element/volume methods that include fluid dynamics effects seem to be more accurate than those that exclude the fluid flow effects. However, commercially available CFD software for LPBFAM is largely limited by either its scalability to utilize HPC or the associated high license cost.
C. There are no massively parallel CFD codes that can simulate the solidification for LPBFAM process. A typical LPBFAM process involves ~30 microns powder layer thickness with melt pool width ~150 microns width moving at speeds as high as 1 m/s. Moreover, melting-solidification phenomena occur at sub-microns scale. To perform "brute-force" physics-based numerical modeling, a representable region of interest will require mathematical solutions for tens of billions of non-linear equations of heat transfer, solidification and fluid dynamics. Thus, extensive computational resources are needed to tackle the problem in addition to the extensive computational resources.

Most of the studies on predicting grain morphology based on solidification maps were conducted for heat-transfer-solidification-only (HTS) models, i.e., without including the fluid flow effects. This was partly due to either the lack of comprehensive solidification models that include the fluid flow effects or excessive computational time required to conduct coupled fluid dynamics and solidification simulations (HTS-FD). Recently, several codes are being developed for AM simulation (Bikas et al., 2016 and Schoinochoritis et al., 2017). However, their availability is limited due to software costs or are used internally at research centers.

ORNL has unique expertise in modeling solidification defects using the highly scalable open source code, Truchas. Truchas was developed under the Advanced Simulation and Computing (ASC) program at Los Alamos National Laboratory (LANL) for simulation of metal casting processes (Korzekwa, 2009; Raghavan et al., 2016). Recently, Truchas was customized in an internal funded effort by ORNL to study the heat source distribution for various beam paths for EBM. Since Truchas accounts for the characteristics of laser and essential physics, it was selected for the process modeling of LPBFAM. In this report, single-track laser fusion (STLF) simulations were conducted.

3.1 CONSTITUTIVE EQUATIONS FOR LASER FUSION MODEL

Truchas is an open-source, multi-physics simulation code at continuum length-scales designed to solve large problems on parallel high-performance computing (HPC) platforms (Korzekwa, 2009). The energy transport model in Truchas accounts for alloy solidification. The incident heat flux at any location (x, y) on the top surface from the laser beam is given by the Gaussian profile, as:

$$q"_L(x,y) = \frac{2\,P}{\pi R^2}\, e^{-2\frac{\left(x-x_o(t)\right)^2+\left(y-y_o(t)\right)^2}{R^2}}, \quad (1)$$

where P is the laser power, R is the laser beam radius, and ($x_o(t)$, $y_o(t)$) indicates the position of the center of the laser beam. It is well known that without including the heat flux losses due to the metal evaporation under very high laser energy, the calculated temperatures would be unrealistically high (Lei et al, 2001). Assuming an emission from a gray body, the total heat flux into the top surface – including losses due to natural/forced convection, thermal radiation, and evaporation, is given as:

$$q" = \mathrm{A}_\lambda\, q"_L - h_C(T - T_A) - \varepsilon_\infty \sigma(T^4 - T_A^4) - q_{evap}, \quad (2)$$

where, A_λ, ε_∞, h_C, T, T_A, σ, are the absorptivity of the alloy surface at the wavelength of the laser, *total* hemispherical emissivity of the top surface, heat transfer coefficient, surface temperature, ambient temperature, and Stefan-Boltzmann constant, respectively. The evaporation model, which was implemented in Truchas as part of our project, was based on evaluating: (a) the saturated vapor pressure of liquid alloy using the Clausius-Clapeyron equation, and (b) the heat flux loss due to evaporation, q_{evap}, of a mass flux given by the Hertz-Knudsen-Langmuir equation (Glang, 1970) as a function of the latent heat of evaporation, L_{evap}, molecular weight, M, surface temperature, T_s, saturated vapor pressure, and universal gas constant, R, as:

$$q_{evap} = L_{evap}\beta p_o \exp\left[-\left({}^{1}/_{T_s} - {}^{1}/_{T_o}\right) L_{evap}\, M/R\right] \sqrt{\frac{M}{2\,\pi\, R\, T_s}}, \qquad (10)$$

where p_o is the reference ambient pressure, and saturation temperature, $T_o = T_{sat}(p_o)$. *Here,* β is an empirical coefficient which was introduced to accounts for condensation effects.

Projection (or, fractional-step) algorithms for solving the Navier-Stokes equations are composed of advection – or predictor – step and projection step (Bell et al., 1989; Almgren et al., 1996). These projection-based solution algorithms for fluid flows were implemented in the Telluride and Truchas codes (Bell et al., 1989; Reddy et al. 1997). The projection method was adapted to interdendritic flows based on variable-density projection methods (Bell et al., 1992) in Sabau et al. (1999) and Sabau and Viswanathan (2002) by introducing an additional projection variable to (a) exactly enforce the constraint given by mass conservation by applying the projection to the volumetric-averaged momentum of the convected alloy and (b) treat implicitly the drag terms in order to remove the severe time step restrictions associated with semi-implicit discretization.

Thermo-capillary forces due to the surface tension variation and large temperature gradients across the molten metal surface, are the main driving force for fluid flow during LPBFAM. Thermo-capillary forces were first considered in flat-surface models, in which the molten alloy surface was held fixed, i.e., imposing no-flow boundary condition in the direction normal to the surface. In order to simplify the modeling of surface tension effects on free-deformable surfaces, the Continuum Surface Force (CSF) method was developed by transforming the interfacial surface force into a volume force in the region near the interface (Brackbill et al., 1992; Francois et al., 2006). The CSF model was first implemented in the LANL codes, including Truchas. The specific implementation of the thermo-capillary forces, i.e., Marangoni forces, was described in Francois, Sicilian, and Kothe (2006). Although the full VOF and CSF free-surface models are well established and available in Truchas, their extension to processes that include phase changes, such as casting and welding, by including specific formulations for those cells in the semisolid (mushy) state is not completed. CFS models for handling these mushy zone cells and adhesion of fluid/semi-solid cells to its solid phase are being developed. Saldi (2012) conducted a comprehensive review on flat-surface models for surface tension effects for welding applications. The flat-surface assumption for thermo-capillary forces was extensively used for welding, including those laser-based (Chan et al., 1984; Chan et al., 1987; Choo et al., 1992; Pitscheneder et al., 1996; Chan et al., 1983; Mishra and Debroy, 2005; Ribic et al., 2008; and Saldi 2012). For welding, there are few studies that compare the results for non-deformable surface with those from fully free-surface models (Thompson and Szekely 1989; Ha and Kim, 2005; Saldi 2012). As reported by Saldi (2012), most of the flat-surface laminar models used for welding employed multiplier factors for the thermal conductivity and the viscosity in order to obtain a good agreement with the measured weld pool shapes (Choo et al. 1992, Choo and Szekely, 1994), Mundra and DebRoy 1993), Pitscheneder et al. 1996). On the other hand, even for flat-surface models, the addition of turbulence models for fluid flow was found to improve the agreement with the measured weld pool shapes (Choo and Szekely, 1994; Hong et al., 2002; and Hong et al., 2003).

To the best of our knowledge there were no LPBFAM simulations in which the fluid flow effects were considered. In this study, as a step toward a comprehensive multi-physics LPBFAM model, the laminar fluid flow is considered while the molten alloy surface is assumed to be flat and non-deformable. Even though for laminar flow, the flat-surface assumption is expected to

under-predict the weld pool depth for IN625with negative surface tension coefficient (Saldi, 2012), important insights can be obtained on the effect of fluid flow on the solidification during LPBFAM.

To be concise, only the equations related to the implementation of the surface tension algorithm are given in this study. The surface tension force term in the tangential direction, $\mathbf{FS}^{(T)}$, appears in the predictor step of the projection-based algorithm, in which an intermediate velocity, $\mathbf{u}^*$, is computed from the momentum equation as:

$$\rho\left(\frac{\mathbf{u}^*-\mathbf{u}^n}{\Delta t}+\mathbf{u}\cdot\nabla\mathbf{u}\right)=\mu\,\nabla^2\mathbf{u}^n+\rho\beta_o(T-T_o)\mathbf{g}-\rho_S\mathbf{u}^n\,\frac{\partial g_L}{\partial t}-g_L C_D\mathbf{u}^*+\mathbf{FS}^{(T)}, \quad (3)$$

where ρ is the liquid alloy density, Δt is a time step, μ is the dynamic viscosity of the fluid, g_L is the volumetric fraction of the liquid, and C_D is a drag term that accounts for the Darcy's and Forchheimer's terms (Sabau and Viswanathan, 2002), and superscripts "n" indicates the variables at the previous time level. Although the interdendritic flow was not considered in this study, the Darcy's and Forchheimer's terms were included in the Eq. (3) for the sake of completeness. The Navier-Stokes equation is solved for all the computational cells in which the liquid fraction is above a given coherency threshold value, g_L^{coh}:

$$g_L \geq g_L^{coh} \text{ (for fluid cells)} \quad (4)$$

The default value for g_L^{coh} in Truchas was considered to be 0.01. All the fluid flow simulations were conducted using this default value for the g_L^{coh}, unless otherwise noted.

Surface tension varies linearly with temperature, while density variation with temperature is considered by using the Boussinesq approximation (β_o is the coefficient of thermal expansion). All the properties are listed in the appendix D, where the input file is given. For a flat-surface normal to the Z-axis of the system of coordinate, the components of the $\mathbf{FS}^{(T)}$ are non-zero only in the cells on the top surface and are given as:

$$\mathbf{FS}^{(T)}=\frac{d\sigma}{dT}\left(\frac{\partial T}{\partial x},\frac{\partial T}{\partial y},0\right). \quad (5)$$

Because the interface is flat and constant (having zero curvature), the surface tension force has only a tangential component. Thus, the projection step is comprised of the following update of the total pressure, $P=p+\rho\,g\,h$, and velocity:

$$\nabla\cdot\left(\sigma_p\nabla P^{n+1}\right)=\frac{1}{\Delta t}\nabla\cdot(\rho\,g_L\mathbf{u}^*) \text{ and } \rho\,g_L\frac{\mathbf{u}^{n+1}-\mathbf{u}^*}{\Delta t}=\sigma_p\nabla P^{n+1}, \quad (6)$$

where the projection variable is given by:

$$\sigma_p=\frac{g_L}{1+g_L\,C_D\Delta t/\rho}. \quad (7)$$

The implementation in Truchas of the thermo-capillary model was validated by Francois, Sicilian, and Kothe (2006) against analytical results of Bauer and Eidel (2003) for a "rigid-lid" cavity problem, in which a free-slip boundary condition was imposed for velocity at the fixed free-surface and a linear distribution of temperature between the two differentially heated walls was imposed.

3.2 EVALUATION OF MICROSTRUCTURE FROM LPBFAM SIMULATIONS

Solidification in LPBFAM process governs the size and morphology of microstructure features, such as primary arm spacing and the extent of micro-segregation, which in turn affect the properties of the additively manufactured parts. The microstructure types and its length-scales were shown to be governed by the following variables (Hunt, 1984): local temperature gradient (G), solidification velocity (V), and combinations thereof: the cooling rate (dT/dt, or GV) and G/V. While G/V can be used to assess the type of the solidification front (planar, cellular, or dendritic), GV (cooling rate) controls the size of the solidification structure (Kurz and Fisher 1998; Rappaz and Dantzig, 2009; Raghavan et al. 2016, Raghavan et al. 2017, and Ghosh et al., 2018). The temperature gradient (G) is calculated, as:

$$G = \sqrt{G_x^2 + G_y^2 + G_z^2}, \tag{8}$$

where G_x, G_y and G_z are temperature gradients along X, Y and Z directions, respectively. The solidification velocity, or growth rate, is calculated as the ratio between cooling rate, dT/dt, and temperature gradient, as:

$$R = \frac{dT}{dt}\frac{1}{\mathrm{G}}. \tag{9}$$

Although the laser-based AM processes feature nominally a smaller beam size, e.g., 100 microns, the solidification-related variables G and V were found to vary within the solidified melt-pool, which is of sub-millimeter length-scale. From heat-transfer and solidification simulations that excluded fluid dynamics effects, it was found that both G and V increase as the melt-pool becomes smaller with increasing the laser scan speed, U (Ghosh et al. 2018). On the other hand, G decreases as the melt-pool becomes larger with increasing laser power, P, for a constant laser scan speed, U. It was found that low V's and high G's exist at the bottom of the melt-pool whereas a higher V's and lower G's exist close to the melt-pool surface (Ghosh et al., 2017). It is, thus, very important to assess the variation of the microstructure related variables, G, V, G/V, and GV over the solidified melt-pool, in order to understand the microstructure variation in LPBFAM process.

An analytical model was developed by Hunt (1984) to understand the columnar-to-equiaxed transition (CET) in welding processes. Hunt's CET model relates the thermal gradient (G), growth rate (V) and volume fraction of equiaxed grains (Φ) during solidification. The columnar-to-equiaxed transition (CET) was considered to occur when the volume fraction of equiaxed dendrites would reach a certain value to block the growth of the columnar dendrites. According to the Hunt (1984) criterion, the (G, V) thresholds for CET can be obtained using certain volume fraction of equiaxed dendrites at the growth interface of columnar dendrites under different growth conditions. Gäumann *et al*. (2001) extended the theory using the Kurz-Giovanola-

Trivedi (KGT) model for rapid solidification processes by neglecting the nucleation undercooling (ΔT_n) at high thermal gradients (e.g., 10^6 K/m) and simplified the model, as:

$$\left(\frac{G^n}{V}\right) = a\left\{\left(\frac{-4\pi N_o}{3\,ln(1-\Phi)}\right)^{\frac{1}{3}} \cdot \frac{1}{n+1}\right\}^n, \tag{10}$$

where N_o is the number of nucleation sites, Φ is the volume fraction of equiaxed grains, n and a are alloy-dependent constants. Number of nucleation sites and volume fraction of equiaxed grains can be determined from experimental observations. Without having experimental data on the number of nucleation sites, the CET curves used in this study for IN625 were those obtained by Hu et al. (2018) at volume fraction of equiaxed dendrites of 0.66% and 49%, as shown in Figure 1: (a) the area above the dotted line (49% fraction of equiaxed dendrites) corresponds to the fully equiaxed dendrites zone; (b) area below the dash-line (0.66% fraction of equiaxed dendrites) corresponds to the fully columnar dendritic microstructure; and (c) area between the dotted line and dash line would exhibit mixed (equiaxed and columnar) dendritic microstructure.

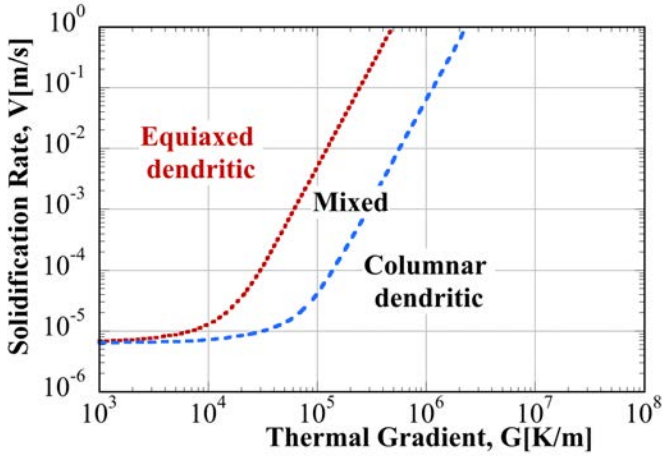

Figure 1. (G, V) microstructure selection map based on Hunt's model for IN625.

In this study, the solidification microstructure-related variables (G, V, G/V, and G V) were obtained during the simulation with the Truchas code. For CET prediction based on (G, V) microstructure maps, the G was evaluated at a fraction solid f_S=0.05, which is close to the liquidus temperature (Nastac, 2004). For calculation of primary dendrite arm spacing (PDAS), the G is usually averaged over most of the solidification interval, i.e., f_s=0.05 to 0.95.

3.2.1 Correlations for primary dendrite arm spacing (PDAS)

The dependence of PDAS (λ_1) on G and V was reviewed by Ghosh et al. (2017) for Ni superalloys, where experimental data was referenced (Bouse and Mihalisin, 1989; and Whitewell et al., 2000). Based on Hunt (1979) and Kurz and Fisher (1981), the power law dependence can be written in a general form, as

$$\lambda_1 = A_o\, G^{-m}\, V^{-n}, \tag{11}$$

where m and n are positive exponents. Analytical expressions for constant A_o as a function of material properties were derived by assuming spherical or ellipsoidal dendrite tips (Hunt, 1979, and Kurz and Fisher, 1981, respectively). In these analytical models, the exponents in Eq. 10 were m=0.5 and n=0.25. Another power law for the PDAS dependence was shown to be simply $(G\ V)^{-m}$ (Whitewell et al., 2000). Keller et al. (2017) showed for IN625 that Hunt's model yields PDAS values closer to the experimental values than Kurz-Fisher model, using G and V values from heat-transfer-and-solidification simulations, similar to the HTS model in this study. Keller et al. (2017) also indicated that neither Hunt's model nor Kurz-Fisher's model provides an "objective good fit" as the dendrite tips under severe solidification conditions may differ than the spherical or ellipsoidal shapes assumed in the development of these models. In Hunt's model, $A_o = A\ (k\Gamma\Delta T_o D_L)^{0.25}$, where k is the partition coefficient, Γ the Gibbs Thomson coefficient, ΔT_o the equilibrium freezing range, D_L the diffusivity of the liquid.

Ghosh et al. (2018) used G and V values from heat-transfer-and-solidification simulations of single-track laser scan on bulk IN625 to identify that an appropriate range for the model constant A in Hunt's model was between 1.3 and 1.7. Using the following values for the material properties of IN625 - k=0.48, Γ = 2.2e-7 K m; ΔT_o=60 K, and D_L=3.0e-9 m^2/s (Ghosh et al. 2018) – the factor $(k\Gamma\Delta T_o D_L)^{0.25}$, was estimated to be 3.7131e-4 $(K^2m^3s^{-1})^{0.25}$; where the engineering E-notation was used to specify the values of each variable, i.e., 1.2e-9 would mean $1.2x10^{-9}$.

Considering a mean value of A of 1.5 for Hunt's model constant, the constant A_o in Equation 10 was evaluated and PDAS equation becomes $\lambda_1[\mu m] = 557\ G[K/m]^{-0.5}\ V[m/s]^{-0.25}$. We have to emphasize that this correlation was developed using calculated values for G and V from an HTS model, without considering fluid dynamic effects. Thus, this analytical PDAS expression is an acceptable initial correlation. This analytical expression has to be recalibrated when material properties used in the HTS model would be different than those used by Ghosh et al. 2018 and Keller et al. (2017), as G and V would be different.

3.3 EXPERIMENTAL DATA FOR SINGLE-TRACK LASER FUSION

Melt-pool geometry and microstructure data for single-track laser fusion (STLF) experiments, which was obtained at GEGR, was provided as in-kind for this project. For IN625, the melt-pool shape was found to be similar in both powder and fully-dense substrate cases (Ghosh et al., 2018), although the laser powder bed fusion exhibited additional width and height variations due to handling of the powder particles. Thus, experiments for single-track laser fusion on fully-dense bulk material are a precursor to the LPBFAM. Moreover, the microstructure for single-track laser is representative for the LPBFAM process as the bottom part of the melt-pool would consist of re-melted and re-solidified bulk material, which is below the powder-bed, resulting in similar solidification conditions as those for STLF. The laser beam diameter was set to 80 microns, unless otherwise noted.

Two batches of cases were selected to assess the fluid dynamics effects on the melt-pool and microstructure. The first STLF batch comprises one case with a melt-pool dominated by conduction and another case with an elongated, keyhole melt-pool (Table 1). These two cases would be used to assess if the STLF can predict the key-hole melt-pools. The low-resolution optical micrographs for the melt-pool are shown in Figure 2. The second STLF batch consists of 4 cases (Table 2), all with different laser power and scan speed levels that yield different primary

dendrite arm spacings (PDAS). The high-resolution SEM micrographs for the melt-pool are shown in Figure 3. These SEM pictures were sized to scale, i.e., the 20 micron marker has the same length in all the four figures.

Table 1. Single-track laser fusion cases in the conduction and key-hole regime considered for melt-pool assessment.

Case	***File name***	***Power [W]***	***Speed [mm/s]***	**Exp. Melt-pool width *[um]***	**Exp. Melt-pool Depth *[um]***	***Regime***
1	*mp1*	*100*	*300*	132	46	Conduction
2	*mp2*	*150*	*300*	196	168	Key-hole

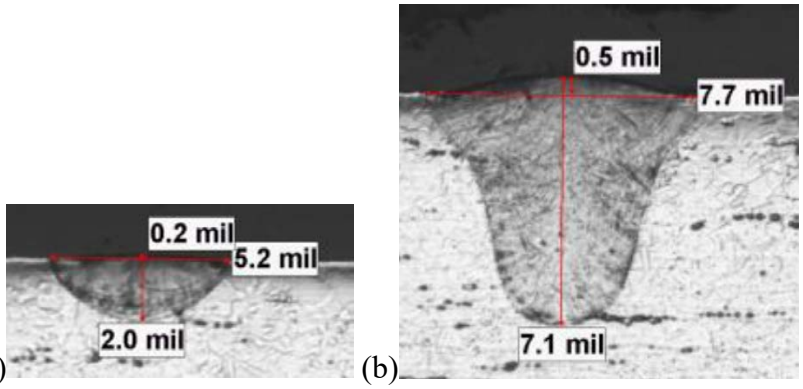

(a) (b)

Figure 2. Optical micrographs of the melt-pool for a single laser track experiments: (a) mp1 and (b) mp2 cases.

Table 2. Single-track laser fusion considered for melt-pool assessment and microstructure analysis in the conduction regime.

Case id	**Power [W]**	**Speed [mm/s]**	**Exp. Melt-pool width [um]**	**Exp. Melt-pool Depth [um]**	**PDAS [um]**
p2s05	75	50	158	58	0.99
p2s1	75	100	131	49	0.72
p2s2	75	200	110	39	0.60
p4s6	150	1000	89	31	0.50

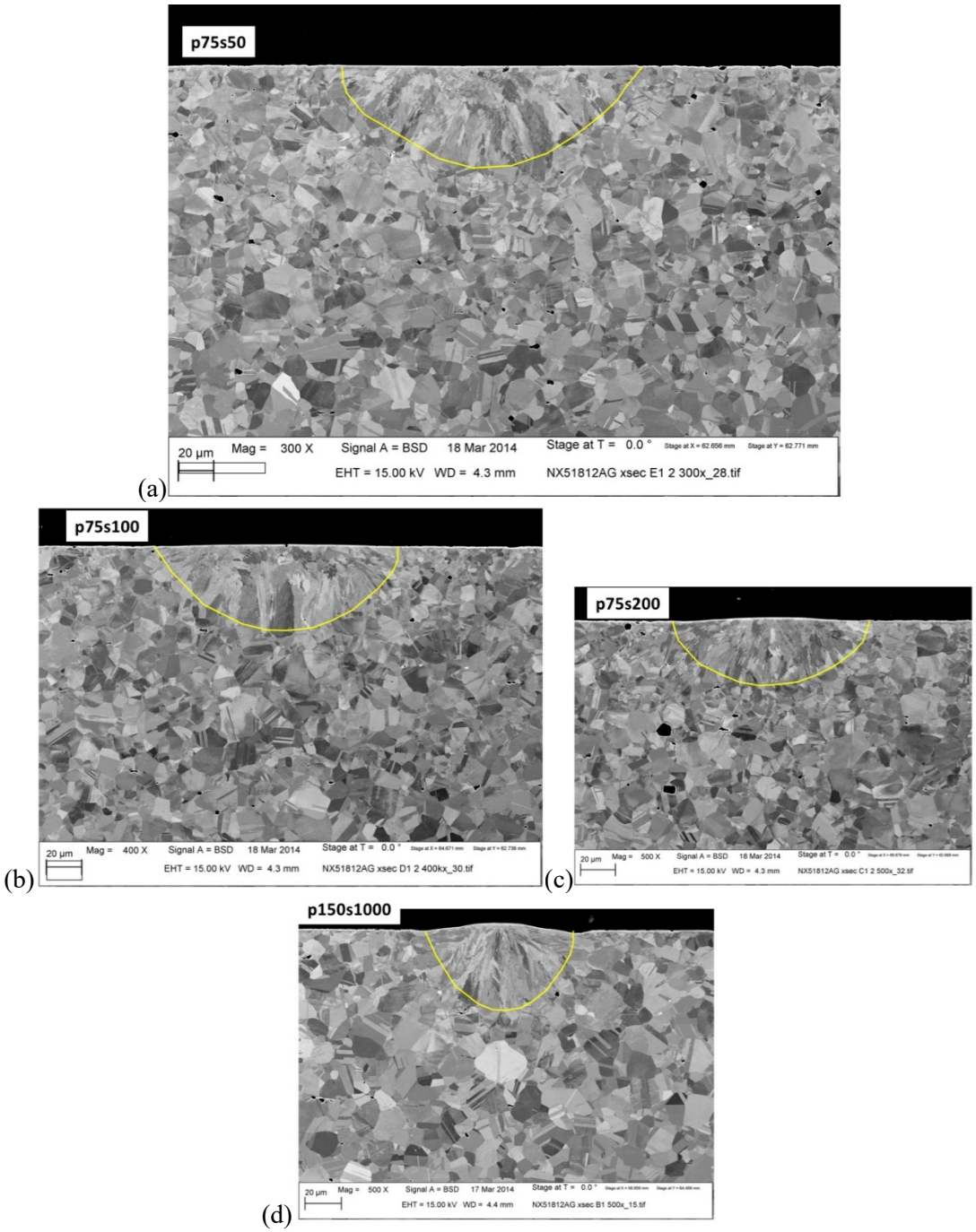

Figure 3. SEM micrographs of the melt-pool in bulk material for single laser track experiments: (a) p2s05, (b) p2s1, (c) p2s2, and (d) p4s6.

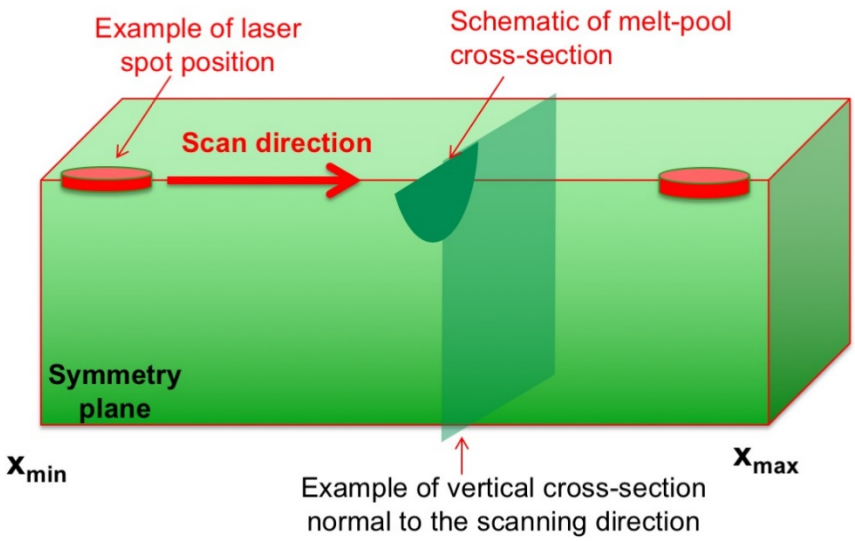

Figure 4. Vertical cross-section normal to the scan direction where melt-pool microstructure images were taken.

3.4 SETUP OF STLF SIMULATION MODEL AND MATERIALS PROPERTIES

Two types of models are considered for the simulations, with and without the fluid dynamics effects, HTS-FD and HTS, respectively, as illustrated in Table 3.

Table 3. Simulation types to assess fluid dynamics effects on STLF simulations.

Model type	*Heat Transfer	Evaporation	Fluid Flow	**Surface-tension	Free-moving surface	Recoil Pressure
HTS	Y	Y	-	-	-	-
HTS_FD	Y	Y	Y	Y	-	-

*includes: (1) evaporation, (2) latent heat release due to phase changes (melting/solidification), and (3) evaluation of microstructure-related parameters (G, V)
**Flat-surface

Thermo-physical properties required at input for the numerical simulations were selected based on literature review or were calculated based on thermodynamic simulations using JMatPro software (Saunders et al., 2003). Valencia and Quested (2008) reviewed the thermophysical property data for Ni superalloys. Mills et al. (2006) provided property relationships as a function of alloy composition. Thermophysical property data is given Appendix A for specific heat, thermal conductivity, viscosity, and surface tension. The temperature dependence required in the Truchas input file as a power-law polynomial are given in Appendix D.

There was no experimental data found in the literature on coefficient of surface tension specifically for IN625. The JMatPro calculated data on coefficient of surface tension, $d\sigma/dT$, was found to vary between -4e-4 N/m at liquidus to -2.4e-4 N/m at temperatures above 2,500 C (Appendix A). The experimental data for $d\sigma/dT$ of Ni superalloys (CMSX-4, IN738LC, MM247LC, and C263) was found to vary between -6.8e-4 N/m to -15e-4 N/m (Aune et al., 2005

and Matsushita et al., 2011). For IN718, dσ/dT was measured to be -1.1e-4 N/m (Mills et al., 2006). This range of reported values for dσ/dT are fairly close to those estimated based on JMatPro simulation data.

A short literature review is presented here on optical properties that were not evaluated using the JMatPro software. A literature review on materials properties for IN625 indicated that emissivity and absorptivity exhibited a wide range of reported values. Two optical properties are required for the simulation: hemispherical emissivity for thermal radiation losses and absorptivity at the laser wavelength, A_λ. Measured data on hemispherical emissivity of bulk IN625 was reported to be increasing with temperature from 0.32 to 0.38 at temperatures of 370 and 925 ^oC (Compton, 1986). However, the emissivity of oxidized and rough surfaces would be much higher. Keller et al. (2018) did not explicitly give a value for emissivity. In this study, an emissivity of 0.7 was considered for thermal radiation losses.

Keller et al. (2018) used A_λ=0.5 for modeling the LPBFAM of IN625 alloy. For an Inconel alloy (79.5 Ni, 13.0 Cr, 6.5 Fe, and 0.08 C), the absorptivity at 1.06 um wavelength was estimated using a validated Drude model (Chen and Ge, 2000) to be approximately 0.24 at temperatures of 120 to 600 ^oC (Boyden and Zhang, 2006). Using the following relationship between the absorptivity and resistivity r(T), (Bramson, 1968; DebRoy and David, 1995):

$$A_\lambda(T) = 0.365\sqrt{\frac{r(T)}{\lambda}} - 0.0667\frac{r(T)}{\lambda} + 0.006\left(\frac{r(T)}{\lambda}\right)^{1.5}, \quad (12)$$

the absorptivity for IN625 was estimated to be 0.33 at 1.064 um wavelength and a resistivity of 1.3e-4 Ohm cm.

In this study, a single laser scan line was simulated until uniform steady-state conditions were reached. Using symmetry on the centerline of the scanline, the computational domain was set to 1.1, 0.5, and 0.4 mm in the scan direction (X), lateral direction (Y), and depth (Z), respectively. The mesh used is shown in Appendix B. Within the overall domain, a subdomain in which the melt-pool is expected to develop was further refined. The length of the high-resolution subdomain was of 0.709, 0.103, and 0.072 mm in the X, Y, and Z directions (Appendix B). The mesh resolution in the high-resolution subdomain was 4.07, 2.65, and 1.85 microns in X, Y, Z directions, respectively. The boundary conditions for the computational domain are indicated in Figure 5. The simulation setup for Truchas simulations is presented in Appendix C. The entire Truchas input file is included in Appendix D.

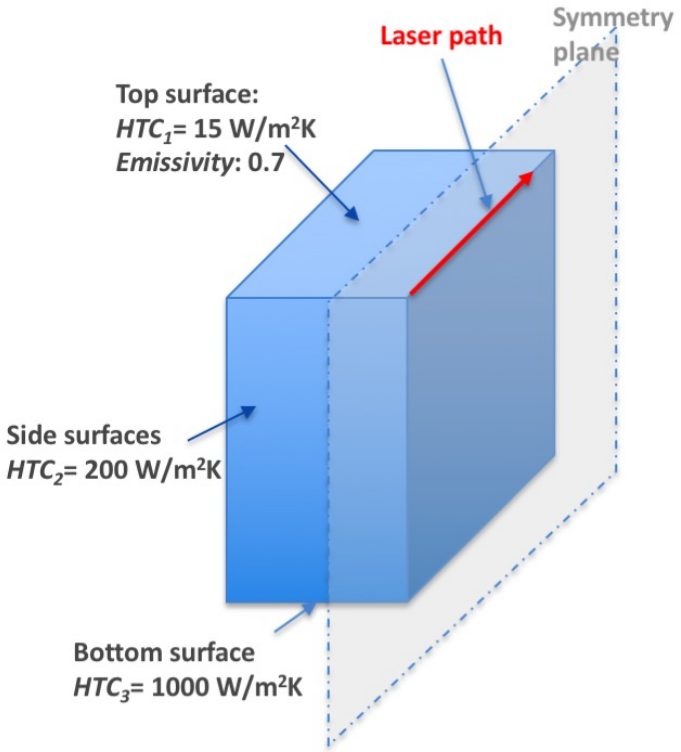

Figure 5. Computational domain for LPBFAM simulations identifying heat transfer boundary conditions.

3.5 DUAL-SIMULATION AT MELT-POOL AND COMPONENT LENGTHS-SCALES

A global-master simulation and local simulation were envisioned to reduce the CPU time required to simulate LPBFAM (Figure 6). The main master Truchas simulation would consist only simulating the heat transfer-and-solidification while exchanging and storing detailed information from the micro-simulation on microstructure-related variables, such as thermal gradient, G, and solidification velocity, V.

The local simulation will include the fluid dynamic effects on the laser melting process solidification models at the micro-scale in addition to the heat transfer (and latent heat release due to melting/solidification). For the local simulation, two approaches were considered for evaluation: (a) in the Lagrangian approach, the local simulation would consist of a controlled volume that is continuously moving with the laser beam; and (b) in the Eulerian approach, the local simulations will be activated as the laser beam moves across specific controlled volumes. The local simulations will be truly HPC simulations in order to speed up the simulations. Local-simulations would be limited to the 3x wide and 6x length the beam size while the height will be dynamically allocated to include 2x the liquid pool size. The local simulations would need the get the data on temperature distribution prior to their onset.

The main master Truchas simulation would consider only the heat transfer while exchanging and storing detailed information from the micro-simulations on microstructure length-scales. Thus, the fluid dynamics effects on the LPBFAM would be considered without excessive CPU expense

and loss of accuracy. The local-global approach would enable an efficient allocation of computer resources, e.g., velocity and pressure data fields and ensuing CFD solver data need to be allocated only over a small domain of the beam size length scale.

This approach for conducting dual-simulations at melt-pool length-scales and component lengths-scales is schematically represented in Fig. 6. It was decided to use the Lagrangian approach for the local simulation. The global simulation at component scale will be conducted in a fixed system of reference, while the simulation at melt-pool scale will be conducted with respect to a system of reference attached to the laser beam in order to significantly decrease the CPU time.

Concerning the local simulation implementation, the source code modification of Truchas for a moving system of reference (MSoR) simulation was completed by Alan Stagg and Adrian Sabau at ORNL. The temperature and liquid fraction data from the MSoR simulation is shown in Figure 7 at two locations on the top surface: (a) X=0 (center of the domain) and (b) X=107 um from the center of the domain. The data shows that the uniform steady state is reached after a simulation time of approximately 1.4 ms.

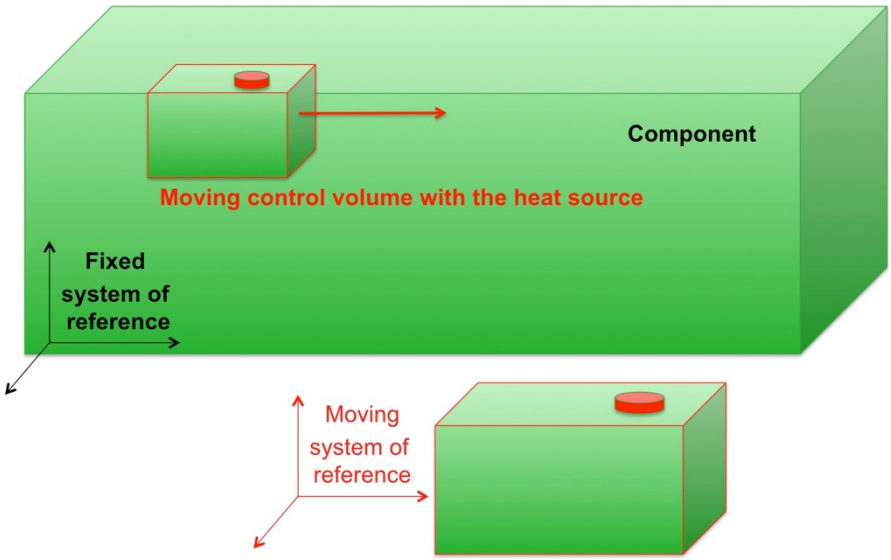

Figure 6. Dual-simulation approach for modeling of Additive Manufacturing.

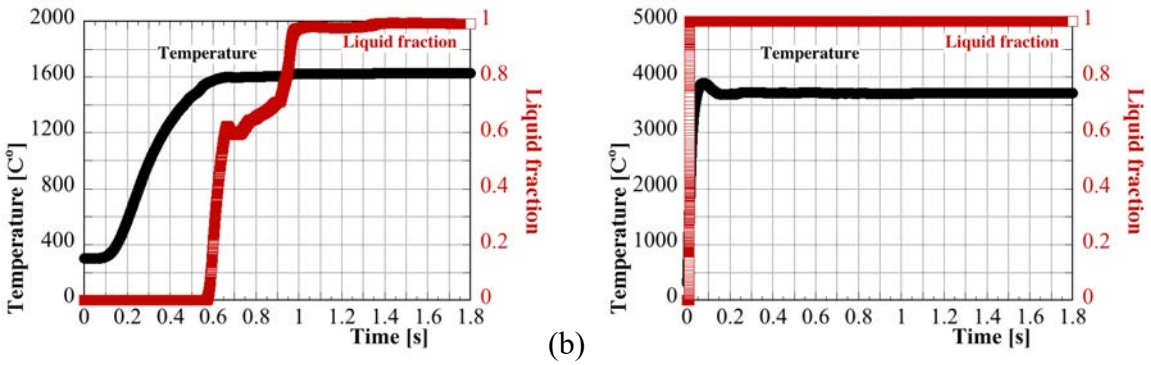

Figure 7. Temperature and liquid fraction from the HTS_FD MSoR simulation at two locations on the top surface of the melt-pool with: (a) X=0, and (b) X=107 um from the domain center.

The HTS_FD simulation in moving system of reference (MSoR) can provide accurate data on the liquid pool shape. However, the liquid pool will never solidify in the MSoR simulation. In order to obtain the thermal gradient, G, and solidification velocity, V, which are required for evaluating the microstructure type, temperature data need to be recreated from the MSoR temperature data into the static, absolute system of reference. Since this data post-processing of the steady-state simulation is not trivial on a multi-processor simulation, the project team made the decision to cease further development in order to obtain useful LPBFAM data within the budget.

3.6 NUMERICAL SIMULATION RESULTS FOR STLF TO ASSESS FLUID FLOW EFFECTS ON MICROSTRUCTURE

In order to validate Truchas for STLF and LPBFAM modeling, experimental data, which was obtained at GEGR for liquid pool shape and microstructure, were compared with those from numerical simulation results at two power levels for a constant scan speed. The results show that the melt-pool shape was affected by the fluid dynamics.

First, the melt-pool dependence on evaporation and surface tension coefficient was studied for a laser absorptivity of 0.5. These STLF simulations were conducted on Titan using 288 CPUs per each run, for a total of 5760 CPUs for the 20 runs that were conducted. Each STLF simulation ran for 12 hours to simulate approximately 2ms of actual STLF processing time.

Second, the melt-pool dependence on beam size, evaporation, and surface tension coefficient for an absorptivity of $A_\lambda = 0.3$ was studied. In total, twenty-five cases were run, fifteen runs for the HTS model and ten runs with the HTS_FD model. Each of the twenty-five runs was conducted on an HPC Linux Cluster (CADES) with 32 CPUs per each run.

3.6.1 Melt-pool dependence on evaporation and surface tension coefficient at a laser absorptivity of 0.5

Numerical simulation results for the temperature evolution at a point located in the center of the beam path is shown in Figure 8, for the *mp1* simulation case considered in Table 1 to illustrate the evaporation effect on the temperature field and ensuing solidification. For this sensitivity study, an absorptivity of A_λ=0.5 at 1.06 um wavelength of the laser was used. The results shown in Figure 8, indicate that not only the peak temperature decreased, but also the solidification time has been reduced.

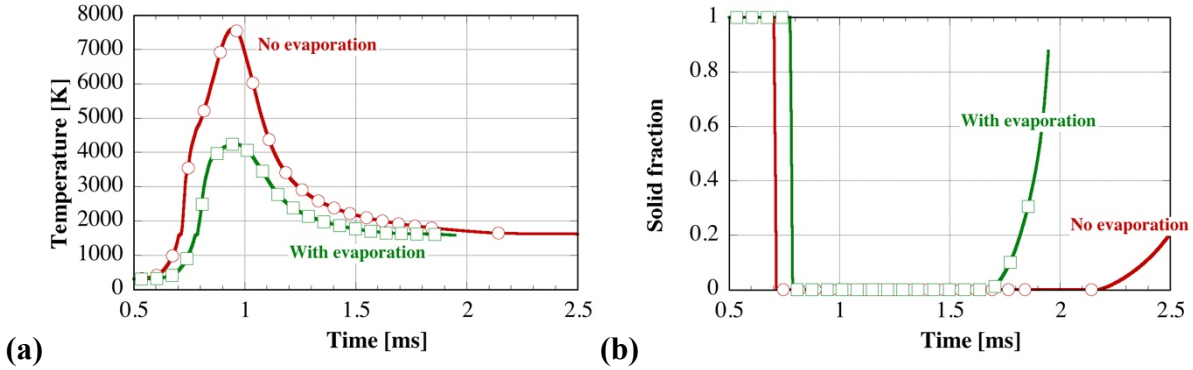

Figure 8. Calculated (a) temperature, and (b) solid fraction at the single-scan centerline to illustrate the effect of evaporation on solidification (HTS simulation, mp1 case, β = 0.1).

In order to validate Truchas for STLF and LPBFAM modeling, experimental data, which was obtained at GEGR for liquid pool shape and microstructure at a constant speed of 0.3 m/s (Table 1), were compared with those from HTS_FD numerical simulation results at two power levels for a constant scan speed. Ten cases were considered for HTS_FD STLF simulations for different values of the surface tension coefficient, dσ/dT, and laser absorptivity, A_λ (Tables 4 and 5).

The calculated melt-pool width, $\mathbf{W_{calc}}$, and melt-pool depth, $\mathbf{H_{calc}}$, are shown in Tables 4 and 5 for the *mp1* case (conduction regime) and *mp2* (keyhole regime), respectively. The corresponding errors of the calculated melt-pool widths and depths with respect to the measured values (W_{exp} and H_{exp}) were calculated, as:

$$W_{error}\,[\%]=100*(W_{exp}- W_{calc}) / W_{exp}, \text{ and } H_{error}\,[\%]=100*(H_{exp}- H_{calc}) / H_{exp} \quad (13)$$

An overall error between the calculated and measured melt-pool dimensions can be simply defined as the average of the absolute values of the errors for the pool width and pool height, i.e., $(abs(H_{err})+ abs(W_{err}))/2$. The errors for the two melt-pool dimensions were shown in the last two columns of Table 4 and 5 for the *mp1* and *mp2* cases, respectively. By comparing the melt-pool data at constant $d\sigma/dT$, the absorptivity was found to slightly increase the melt-pool depth and melt-pool width. The error in the melt-pool depth is very high as compared to that for the melt-pool width, and it is especially very high at 80% for the cases with laser powers of 150 W (i.e., mp1 case in the conduction regime). The error between computed and experimental value for the melt-pool width is lowest for an absorptivity value 0.45 (0.5) and 0.55 for cases with laser powers of 100 W and 150 W, respectively. The error between computed and experimental value for the melt-pool depth is lowest for an absorptivity value 0.55 for cases with laser powers of 100 W, while the error is very high at 80% and virtually unchanged for the cases with laser powers of 150 W. It has to be noted that the results shown in Tables 4 and 5 were obtained with the maximum evaporation rate, i.e., with a value of 1 for β, the empirical coefficient that accounts for condensation effects. For the conduction case, the overall error, $(abs(H_{err})+ abs(W_{err}))/2$, was found to range from 17.9 to 27.6 % (Table 4), with the smallest overall error for the dσ/dT = -2e-4 N/m and A_λ=0.5.

Table 4. Sensitivity of melt-pool geometry on the surface tension coefficient, dσ/dT, and laser absorptivity for the conduction case (β=1) using HTS_FD model.

Case id	Power [W]	dσ/dT [N/m]	A_λ	W_{calc} [μm]	H_{calc} [μm]	W_{error} [%]	H_{error} [%]
mp1b	100	-3e-4	0.45	155.08	31.59	-17	31.3
mp1a	100	-3e-4	0.5	155	31.59	-17	31.3
mp1c	100	-3e-4	0.55	164.34	33.77	-24	26.6
mp1e	100	-2e-4	0.5	177.6	35.96	-14	21.8
mp1a	100	-3e-4	0.5	155	31.59	-17	31.3
mp1d	100	-4e-4	0.5	164.34	31.59	-24	31.3

Table 5. Sensitivity of melt-pool geometry on the surface tension coefficient, dσ/dT, and laser absorptivity for the keyhole case (β=1) using HTS_FD model.

Case id	Power [W]	dσ/dT [N/m]	A_λ	W_{calc} [μm]	H_{calc} [μm]	W_{error} [%]	H_{error} [%]
mp2b	150	-3e-4	0.45	170.86	35.95	12	78.6
mp2a	150	-3e-4	0.5	175.2	35.95	10	78.6
mp2c	150	-3e-4	0.55	177.6	35.95	9	78.6
mp2e	150	-2e-4	0.5	164.36	38.12	16	77.3
mp2a	150	-3e-4	0.5	175.2	35.95	10	78.6
mp2d	150	-4e-4	0.5	177.6	35.95	9	78.6

In an attempt to rule out the fact that the discrepancy might be due to an inappropriate evaporation flux, β, the empirical coefficient that accounts for condensation effects, β, was varied as shown in Tables 6 and 7 from its maximum value of 1 (for the "a" cases), to 0.2, 0.1, and 0.05.

The distribution of the liquid fraction taken at the maximum liquid pool depth location after the uniform steady state was reached is shown in Figure 9, for the conduction cases (i.e., mp1), and in Figure 10, for the keyhole cases (i.e., mp2). For the keyhole cases, the liquid pool shape was found to have a shape common to that of the typical conduction case. From the results shown in Figures 9 and 10, the liquid pool depth and width were obtained and shown in Tables 6 and 7. Due this large error between the calculated pool depth and measured pool depth for the keyhole cases, the keyhole cases were excluded from further analysis in this study.

The results shown in Tables 6 and 7 indicate that the pool width is sensitive to the evaporation flux. The pool depth was found to exhibit a weak dependence on the evaporation factor, β. For the conduction case, the overall error, $(abs(H_{err})+ abs(W_{err}))/2$, was found to range from 20 to 29.4% (Table 6), with the smallest overall error for β=1. It has to be noted that for the simulation of laser processing and welding of superalloys a factor β=0.1 was found to be appropriate.

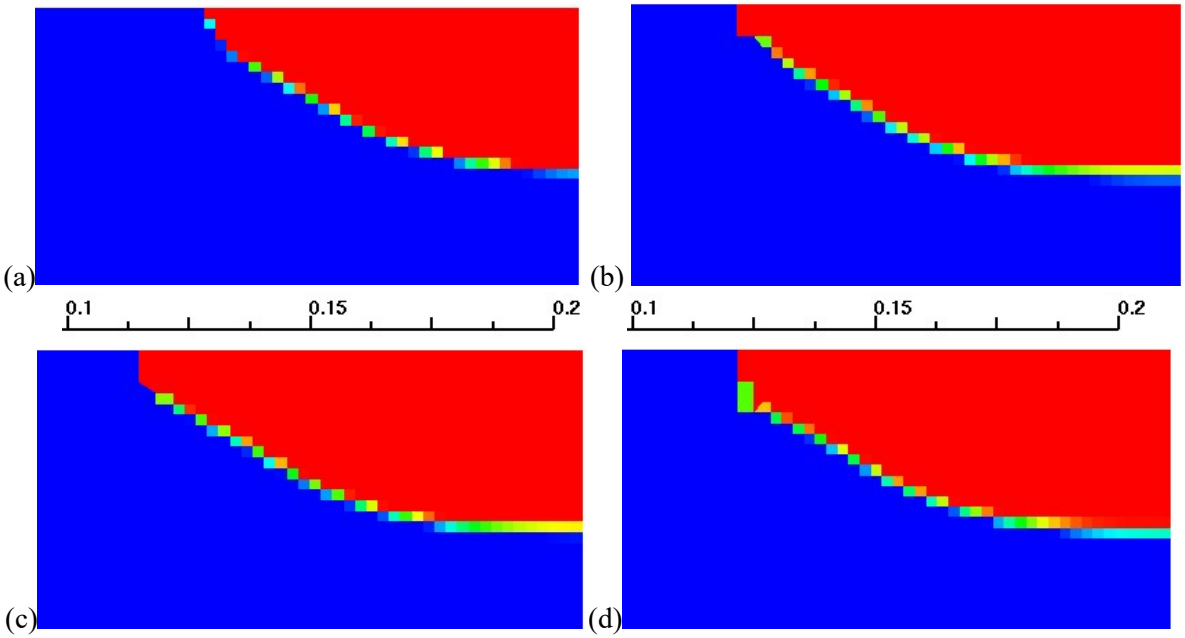

Figure 9. Liquid pool for the conduction dominated cases using HTS_FD model: (a) mp1a, (b) mp1f, (c) mp1g, and (d) mp1h.

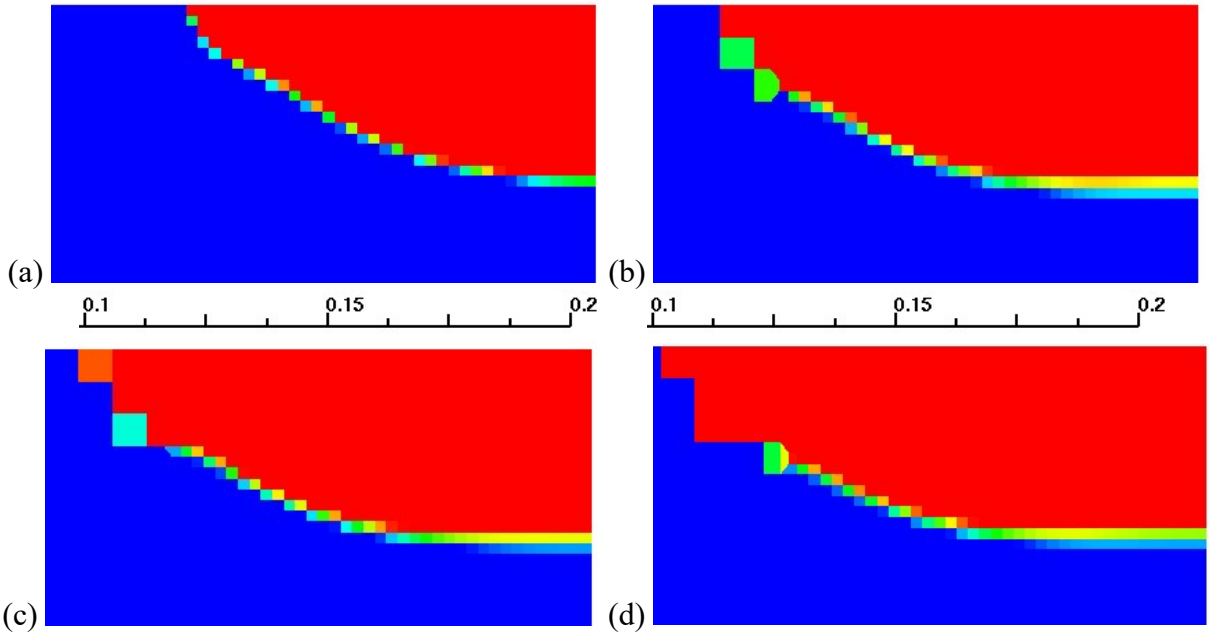

Figure 10. Liquid pool for the keyhole cases using HTS_FD model: (a) mp2a, (b) mp2f, (c) mp2g, and (d) mp2h.

Table 6. Sensitivity of melt-pool geometry on evaporation flux (variable β) for the conduction case ($d\sigma/dT$ = -3e-4 N/m, A_λ = 0.5) using HTS_FD model.

Case id	Power [W]	β	W_{calc} [μm]	H_{calc} [μm]	W_{error} [%]	H_{error} [%]
mp1a	100	1	148	33.2	-12	27.8
mp1f	100	0.2	180	35.5	-36	22.8
mp1g	100	0.1	180	37.9	-36	17.6
mp1h	100	0.05	174	37.9	-31	17.6

Table 7. Sensitivity of melt-pool geometry on evaporation flux (variable β) for the keyhole case ($d\sigma/dT$ = -3e-4 N/m, A_λ = 0.5) using HTS_FD model.

Case id	Power [W]	β	W_{calc} [μm]	H_{calc} [μm]	W_{error} [%]	H_{error} [%]
mp2a	150	1	164	38.7	16	79
mp2f	150	0.2	193	39.5	1.5	79
mp2g	150	0.1	208	41.1	-6	78
mp2h	150	0.05	221	41.1	-12	78

3.6.2 Melt-pool dependence on beam size, evaporation, and surface tension coefficient for a laser absorptivity of 0.3

Table 8 highlights the simulation types conducted to obtain melt-pool dependence on beam size, evaporation, and surface tension coefficient for an absorptivity of A_λ = 0.3. For each of the p2s1, p2s2, and p4s6 cases, four HTS runs and three HTS_FD runs were conducted. Since the case p2s05 was for a very low laser scan speed, which required a much larger simulation time, only one HTS_FD case and three HTS cases were run. Thus, a total twenty-five cases were run, fifteen runs for the HTS model and ten runs with the HTS_FD model. Each of the thirty-two runs was conducted on an HPC Linux Cluster (CADES) with 32 CPUs per each run. The calculated melt-pool width (in μm) and melt-pool depth (in μm) are shown in Tables 9-13.

Initially, two values of 0.5 and 0.1 were selected for the empirical coefficient that accounts for condensation effects, β (Table 9). The corresponding errors between the calculated melt-pool widths and depths were shown in the last two columns of Table 10, respectively. For cases at low laser power of 75 W, the results show that both the pool depth and pool width change with the evaporation flux. Based on preliminary runs for fluid flow with negative surface tension coefficient, $d\sigma/dT$, it is expected that the calculated values from fluid flow simulations would result in increased pool widths and decreased melt-pool depths. For β=0.5, the calculated pool depths were smaller than that the experimentally measured values, and the calculated values are expected to further decrease for the fluid flow simulations. Since β=0.5 is unlikely to yield more accurate results for the fluid flow cases, cases with β=0.5 were further excluded from further evaluation.

For fluid flow HTS_FD model with $d\sigma/dT$ = -3e-4 N/m, the calculated error in the pool width is larger than that of the pool depth (25 to 38% as compared with 17 to 30 %) (Table 10). Since

this error seems to be very large, the sensitivity of the melt-pool shape to the laser beam size was considered next. By increasing the beam size from 80 to 100 μm, the calculated pool width increases beyond its experimental values even for the heat transfer only cases (HTS), especially at higher scan speeds (i.e., cases p2s2 and p4s6 in Table 11). For fluid flow cases with a beam size of 100 um, the calculated pool width was found to deviate by almost 50% from the measured values (Table 12). By decreasing the beam size from 80 to 70 um, the calculated pool depth decreases beyond its experimental values for the heat transfer only cases (Table 13; cases p2s2 and p4s6). The corresponding fluid flow cases for 70 um beam size were not run as the pool depth would be decreasing even further from the already low values calculated in the heat transfer-only simulations. Based on the results presented in Tables 9 to 13, for the HTS and HTS_FD simulations, the initial laser beam size of 80 um was found to be appropriate. Next, the temperature coefficient of the surface tension, dσ/dT, was then decreased from -3e-4, to 1.5e-4, and -0.75e-4. Results for dσ/dT= -0.75e-4 N/mK are shown in Table 14. As compared with the results shown in Table 10 for dσ/dT= -3e-4 N/mK, the decrease in the dσ/dT was found to lower the error in the pool depth, with respect to measured values, to acceptable levels while the pool width error further decreased by approximately 10% (Tables 4 and 9). An overall error between the calculated and measured melt-pool dimensions can be simply defined as the average of the absolute values of the errors for the pool width and pool height, i.e., (abs(H_{err})+ abs(W_{err}))/2. The overall error was found to range from 23.6 to 32.1 % for the results in Table 10 (d_b=80 um, dσ/dT = -3e-4 N/m), from 25.7 to 37.3 % for the results in Table 12 (d_b=100 um, dσ/dT = -3e-4 N/m), from 12.7 to 17.4 % for the results in Table 14 (d_b=80 um, dσ/dT = -0.75e-4 N/m).

Table 8. Simulations types conducted to obtain melt-pool dependence on beam size, evaporation, and surface tension coefficient.

Beam size [um]	**β**	**HTS**	**dσ/dT [N/m] for HTS_FD**
80	0.1	Y	-3e-4
			-0.75e-4
	0.5	Y	-3e-4
100	0.1	Y	-3e-4
70	0.1	Y	-3e-4

Table 9. Calculated melt-pool width and height for d_b=80 um and two evaporation fluxes (β=0.1 and 0.5) using the HTS model.

Case id	**Power [W]**	**Speed [mm/s]**	**W_{calc} [μm]**		**H_{calc} [μm]**		**W_{error} [%]**		**H_{error} [%]**	
			β=0.1	**β=0.5**	**β=0.1**	**β=0.5**	**β=0.1**	**β=0.5**	**β=0.1**	**β=0.5**
p2s05	75	50	142.8	130	62.9	56	9.62	17.7	-8.45	3.45
p2s1	75	100	126.8	118	53.7	46	3.21	9.92	-9.59	6.12
p2s2	75	200	111	98	42.5	37	-0.91	10.9	-8.97	5.13
p4s6	150	1000	90	83	27.77	23	-1.12	6.74	10.4	25.8

Table 10. Calculated melt-pool width and height for d_b=80 um and β=0.1 using the fluid flow HTS_FD model (dσ/dT = -3e-4 N/m).

Case id	**Power [W]**	**Speed [mm/s]**	**W_{calc} [μm]**	**H_{calc} [μm]**	**W_{error} [%]**	**H_{error} [%]**

p2s1	75	100	180.4	36	-37.7	26.5
p2s2	75	200	143.4	32.4	-30.4	16.9
p4s6	150	1000	111	21.6	-24.7	30.3

Table 11. Calculated melt-pool width and height for d_b=100 um and β=0.1 using the HTS model.

Case id	Power [W]	Speed [mm/s]	W_{calc} [μm]	H_{calc} [μm]	W_{error} [%]	H_{error} [%]
p2s05	75	50	157.4	64.8	0.38	-11.7
p2s1	75	100	138.8	55.5	-5.95	-13.3
p2s2	75	200	120	41.6	-9.09	-6.67
p4s6	150	1000	101.8	27.7	-14.4	10.6

Table 12. Calculated melt-pool width and height for d_b=100 um and β=0.1 using the fluid flow HTS_FD model (dσ/dT = -3e-4 N/m).

Case id	Power [W]	Speed [mm/s]	W_{calc} [μm]	H_{calc} [μm]	W_{error} [%]	H_{error} [%]
p2s1	75	100	194	36	-48.1	26.5
p2s2	75	200	148	32.4	-34.5	16.9
p4s6	150	1000	115.6	21.6	-29.9	30.3

Table 13. Calculated melt-pool width and height for d_b=70 um and β=0.1 using the HTS model.

Case id	Power [W]	Speed [mm/s]	W_{calc} [μm]	H_{calc} [μm]	W_{error} [%]	H_{error} [%]
p2s1	75	100	106.5	51	18.7	-4.08
p2s2	75	200	83	37	24.5	5.13
p4s6	150	1000	56	23	37.1	25.8

Table 14. Calculated melt-pool width and height for d_b=80 um and β=0.1 using the fluid flow HTS_FD model (dσ/dT = -0.75e-4 N/m).

Case id	Power [W]	Speed [mm/s]	W_{calc} [μm]	H_{calc} [μm]	W_{error} [%]	H_{error} [%]
p2s05	75	50	196	62.9	-24	-8.45
p2s1	75	100	169	51.8	-29.0	-5.71
p2s2	75	200	137.4	38.8	-24.9	0.51
p4s6	150	1000	100.5	25.9	-12.9	16.5

3.6.3 Distribution of microstructure-related variables within the melt-pool

From numerical simulation results, thermal gradient, G, and solidification velocity, V, were obtained in order to predict the microstructure type (e.g., dendritic, cellular). The spatial distribution of the microstructure variables in a vertical cross-section through the solidified track of liquid pool, normal to the laser scanning direction, were presented for p2s1, p2s2, and p4s6 cases. These simulations were run with the parameters identified in the previous section, as: laser beam size d_b=80 um, absorptivity A_λ = 0.3, empirical coefficient for condensation effects β=0.1, and temperature coefficient of the surface tension, dσ/dT=-0.75e-4 N/m. Unless otherwise noted, the fluid dynamics Equations 3 and 5 were solved in those cells in which the liquid fraction was larger than the coherency threshold of g_L^{coh} of 0.01 (see Eq. 4).

For these three cases, the distributions of the thermal gradient, G, solidification velocity, V, and cooling rate, GV, are shown in Figure 11, 12, and 13, respectively. The same length-scale was used for all the graphs in Figures 11, 12, and 13. The minimum and maximum were selected for each case in order to provide the best visual illustration of each variable distribution. As shown in Figure 11, the thermal gradient, G, was found to exhibit a *maximum* around the edge of the solidified pool and a minimum in the entire central region of the solidified pool for the heat-transfer-only (HTS) model (Figure 11a, c, and e). For the fluid-flow (HTS_FD) model (Figure 11b, d, and f), G was found to exhibit a maximum at the extremity of the solidified pool (at the free surface and not over the entire edge of the solidified pool) and the minimum in the central region below the free surface of the solidified pool (and not at the free surface of the central region).

As shown in Figure 12 for the two cases at 75 W laser power, the solidification velocity, V, was found to exhibit a *minimum* around the edge of the solidified pool and a *maximum* in the central region of the solidified pool for the heat-transfer-only (HTS) model (Figure 12a and 12b). For the fluid-flow model (HTS_FD), V was found to exhibit some oscillations within the melt-pool. At a higher power (case p4s6), V was found to exhibit similar distributions for both HTS and HTS_FD models (Figure 12e and 12f).

As shown in Figure 12, the cooling rate was found to exhibit different distributions for the HTS model for each of the three cases considered (Figure 13a, c, and e), exhibiting a maximum in the melt-pool center for p2s1 case, two-peak value regions (melt-pool center and edge) for p2s2 case, and at the top surface edge of the melt-pool for p4s6 case. For the HTS_FD model at power of 75 W (i.e., cases p2s1 and p2s2), the maxima were located at different locations than those for the HTS model runs. For the p4s6 case, the distribution of the cooling rate is very similar for the HTS and HTS_FD models (Figure 13e and 13f).

The implication of differences in the distribution of microstructure-related variables for the fluid-flow simulations and for the heat-transfer-only simulations will be discussed in other sections of this report.

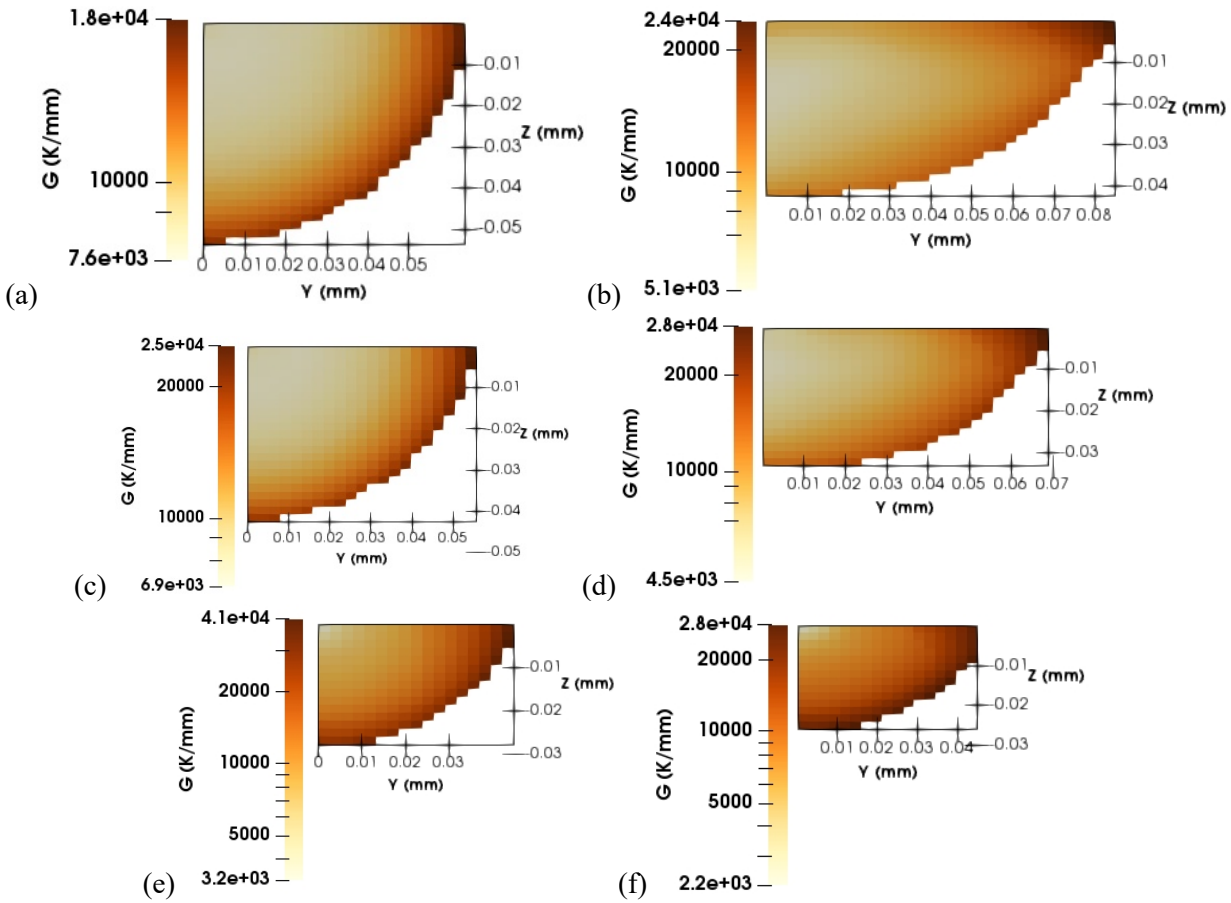

Figure 11. Distribution of thermal gradient, G, for the: (a) p2s1 (HTS), (b) p2s1 (HTS_FD), (c) p2s2 (HTS), (d) p2s2 (HTS_FD), (e) p4s6 (HTS), (b) p4s6 (HTS_FD).

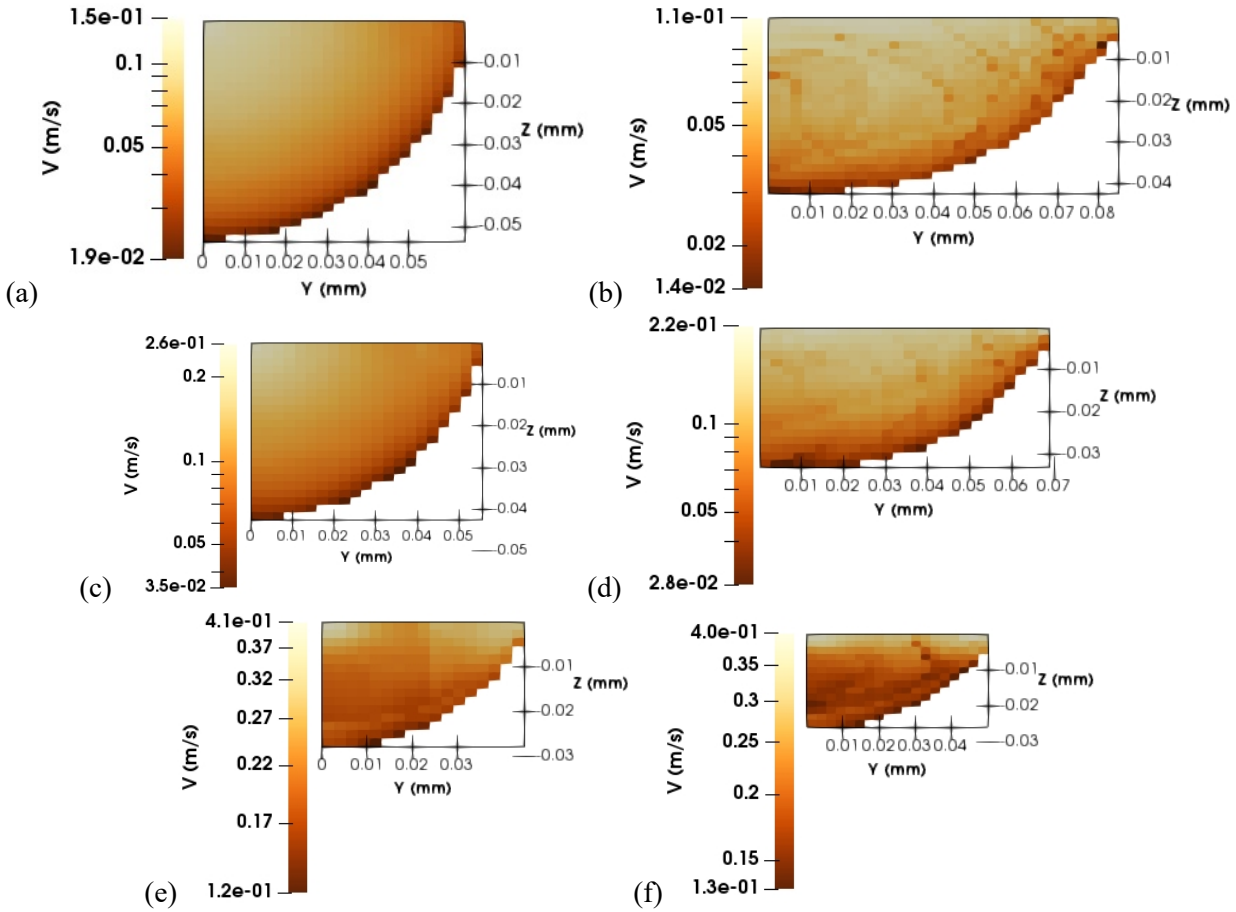

Figure 12. Distribution of solidification velocity, V, for the: (a) p2s1 (HTS), (b) p2s1 (HTS_FD), (c) p2s2 (HTS), (d) p2s2 (HTS_FD), (e) p4s6 (HTS), (b) p4s6 (HTS_FD).

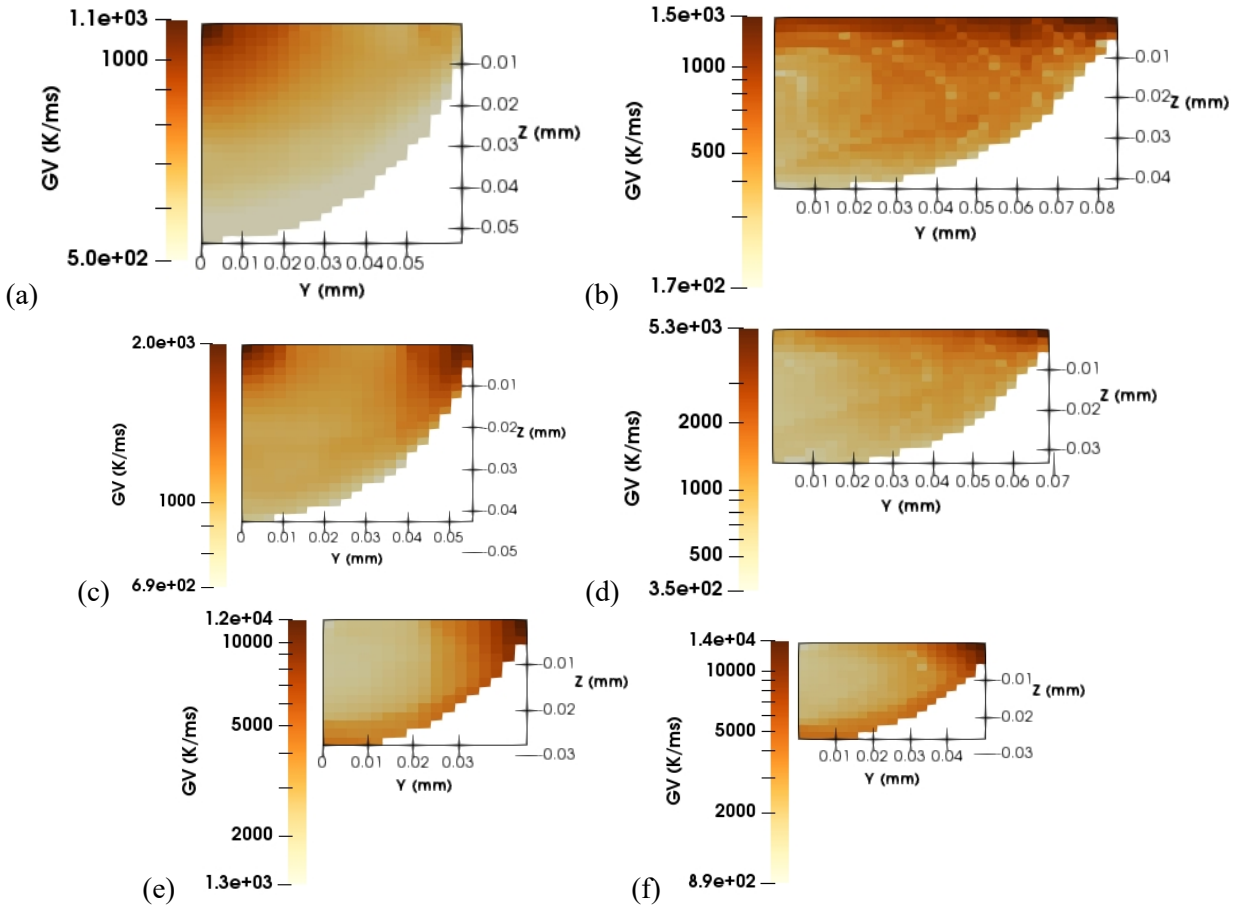

Figure 13. Distribution of cooling rate, GV, for the: (a) p2s1 (HTS), (b) p2s1 (HTS_FD), (c) p2s2 (HTS), (d) p2s2 (HTS_FD), (e) p4s6 (HTS), (b) p4s6 (HTS_FD).

The minimum and maximum values for G, V, and GV, over the entire melt-pool, were summarized in Table 15. The minimum G values for the HTS and HTS_FD simulations are fairly close, with slightly lower values attained for the fluid flow cases (HTS_FD). On the other hand, the maximum G values were observed for the HTS_FD simulations (with the exception of p4s6 case). Both the minimum and maximum values for V were found to occur for the HTS_FD simulations, with the exception of the p4s6 case in which the values were very similar between the HTS and HTS_FD simulations. For the HTS_FD simulations, the minimum values of the cooling rate, GV, were found to be approximately half than their corresponding values for HTS simulations. By contrast with the min GV values, the maximum values for GV were found to occur for the HTS_FD simulations. Thus, HTS_FD simulations were found to exhibit a wider range of cooling rates than the HTS simulations.

Table 15. Minimum and maximum values for G, V, and GV within the melt-pool for HTS and HTS_FD models.

Case	Model	Min G [K/mm]	Max G [K/mm]	Min V [m/s]	Max V [m/s]	Min GV [K/ms]	Max GV [K/ms]
p2s1	HTS	7.6e+3	18.e+3	0.019	0.15	500	1100
	HTS_FD	5.1e+3	24.e+3	0.014	0.11	170	1500
p2s2	HTS	6.9e+3	25.e+3	0.035	0.26	690	2000
	HTS_FD	4.5e+3	28.e+3	0.028	0.22	350	5300
p4s6	HTS	3.2e+3	41.e+3	0.012	0.41	1300	12000
	HTS_FD	2.2e+3	28.e+3	0.013	0.40	890	14000

3.6.4 Computational resources for heat-transfer only simulations and fluid flow

It is important to obtain CPU time needed to run the HTS and HTS_FD models for each case. It is expected that the HTS_FD models would yield more accurate results, as the melt-pool shape is elongated as those seen in the SEM micrographs. This CPU time data will be used to assess the if the additional computational expense for considering the fluid flow phenomena would be worth to obtain more accurate data on the microstructure related variables, thermal gradient, G, solidification velocity, V. For p2s1, p2s2, and p4s6 cases, the CPU time was obtained on a Linux cluster with 32 CPUs. The data show that for the highest speed case considered (p4s6), the CPU time for the fluid flow simulation was approximately 8 times than that for the heat-transfer only simulation. However, the slowest scan speed considered (p2s1), the CPU time for the fluid flow simulation was approximately 65 times longer than that for the corresponding heat-transfer only simulation. We have to mention that implementing simulations in moving system of reference or adaptive meshes will drastically reduce the CPU time required for these simulations.

Table 16. CPU timing for LPBFAM simulations on a Linux Cluster with 32 CPUs.

Case	Scanning speed	Physical simulation time [ms]		CPU [s]	Ratio CPU_FD to CPU_HT
p2s1	100	2.8	HTS	2692	-
			HTS_FD	176020	65.4
p2s2	200	5.6	HTS	3996	-
			HTS_FD	71770	17.96
p4s6	1000	0.64	HTS	3284	-
			HTS_FD	26327	8.02

CPU without microstructure variable post-processing

3.7 ANALYSIS OF MICROSTRUCTURE DISTRIBUTION WITHIN MELT-POOL

From numerical simulation results, thermal gradient, G, and solidification velocity, V, were obtained in a solidification map format in order to predict the microstructure type (e.g., dendritic, cellular). The properties of a part produced by LPBFAM depend strongly on the properties of each single track and each single layer (Yadroitsev and Smurov, 2010). Line-by-line, the laser

beam melts the material along a row of powder-bed and certain bulk material underneath it. Considering the track-by-track and layer-by-layer deposition, the microstructure of the LPBFAM was found to exhibit a layer-wise layout within a vertical cross-section through the build, in which apparent molten pool outline curves can be easily differentiated (Du et al., 2018). Since the microstructural unit of the LPBFAM parts is a single laser melted track, it is worth the study of a single-track, keeping in mind the re-melting of the top bulk layer of material and the re-melting of one corner of the melt-pool due to the overlap during the laser scan for the adjacent layer (Figure 14). Thus, the analysis of the microstructure distribution within a single-track is a focus of this study.

Figure 15 shows a schematic of the representative microstructure region for a single-track melt-pool, indicating the location of vertical lines and horizontal lines along which the calculated data for microstructure-related parameters (G and V) can be conveniently obtained and analyzed for numerous cases.

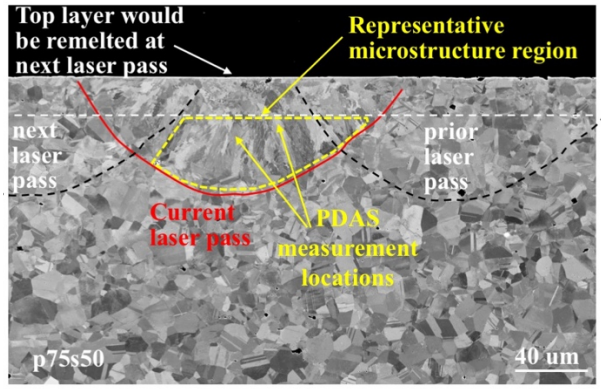

Figure 14. Schematic showing the representative microstructure region within a vertical cross-section of single-track melt-pool.

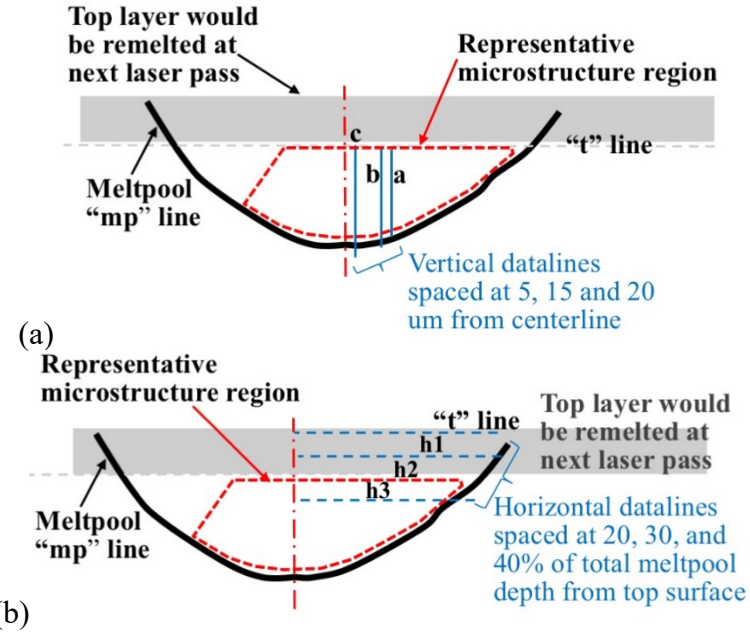

Figure 15. Schematic of the representative microstructure region for a single-track melt-pool. Position of lines in the (a) vertical and (b) horizontal direction along which microstructure-related variables would be obtained.

The data shown in Figures 16 for the thermal gradient, G, and solidification velocity, V, was obtained along five representative data lines, as follow:

- "c" label with "x" symbols represent the data on the vertical centerline (Figure 15a),
- "t" label with circle symbols represent the data on the top surface (Figure 15b), and
- "h1, h2, and h3" labels with triangle symbols that point towards the left, up, and down, respectively, indicate data along the corresponding lines drawn in Figure 15b.

The solidification map data shown in Figure 16, indicate the following:

1. The highest solidification velocity and lowest thermal gradient is located near the region at the top surface in the center of the melt-pool,
2. The smallest solidification velocity is located always near the bottom of the melt-pool in the central region ("c" label with "x" symbols),
3. The fluid flow model results (HTS_FD) exhibited an increased spread in the V(G) variation within the melt pool with respect to the HTS model results (without the fluid flow),
4. The fluid flow model results (HTS_FD) exhibited a decrease in the variation of the solidification velocity with the thermal gradient (i.e., flatter profiles),
5. The p4s6 case exhibit similar results for the HTS and HTS_FD simulations, indicating the fluid flow is not important at high laser scan speeds,
6. For HTS simulations, the data on the vertical centerline ("c" label with "x" symbols) is representative for the variation over the entire meltpool (as similar variations were observed for the data obtained on the horizontal datalines).

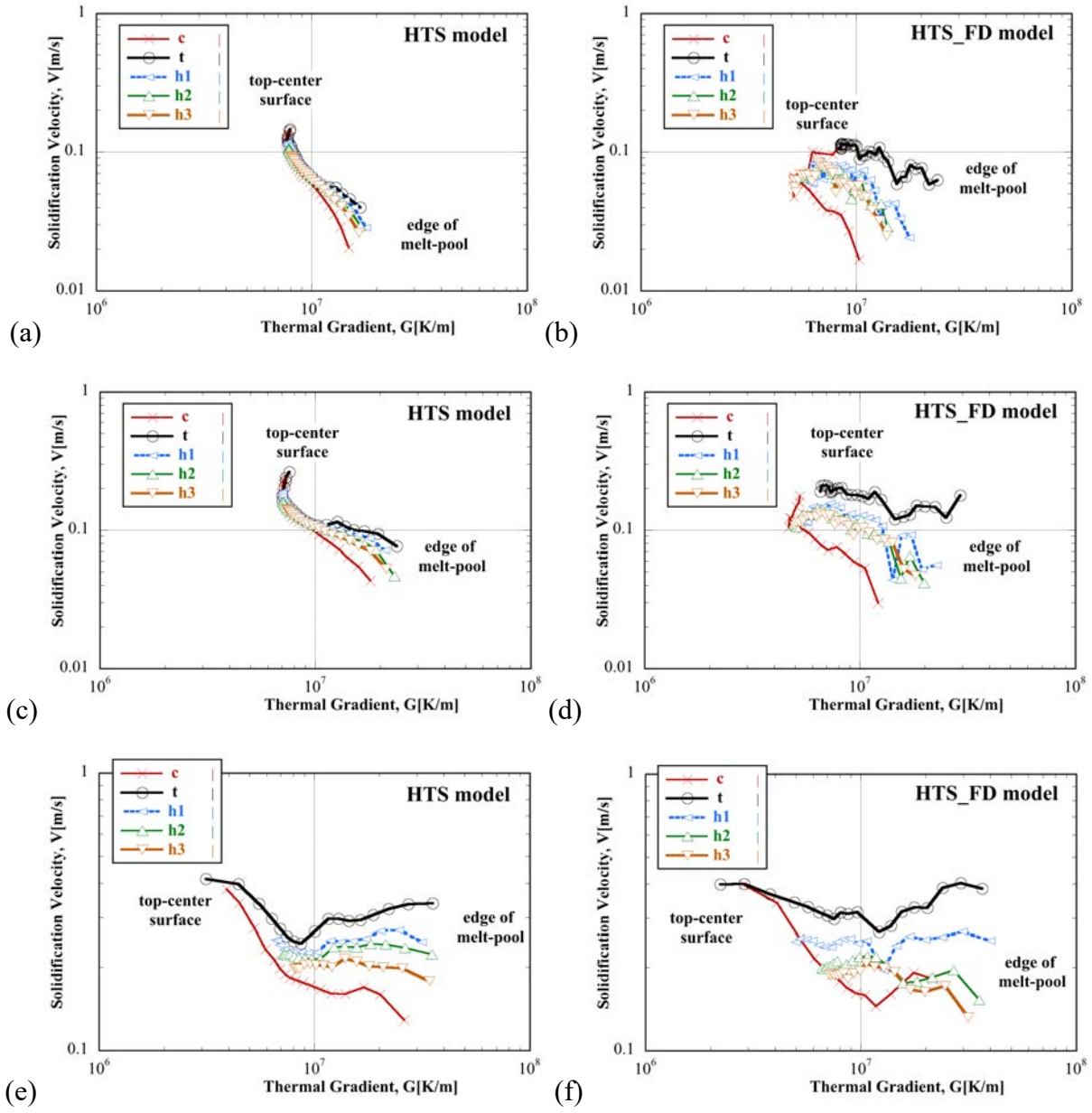

Figure 16. Solidification maps V(G) for: (a) p2s1 (HTS), (b) p2s1 (HTS_FD), (c) p2s2 (HTS), (d) p2s2 (HTS_FD), (e) p4s6 (HTS), (b) p4s6 (HTS_FD).

In order to study the variation in the microstructure length-scale, the estimated PDAS values with Hunt's model with the updated model constants as discussed in Section 3.2.1 are presented in this section. The variation of PDAS is presented along the centerline of the melt-pool in Figure 17, using the (G, V) data shown in Figure 16 with x symbols. The PDAS formula used in discussed in detail in Section 3.2.1. Although this analytical PDAS expression is an acceptable initial correlation, this analytical expression has to be recalibrated as different material properties are used in the HTS model in this study than that used by Ghosh et al. (2018) and Keller et al. (2017). For the sake of simplicity, the PDAS recalibration was not conducted in this study and the PDAS values should be used for identifying the qualitative distribution of

PDAS and not its absolute values. The average PDAS measured for p2s1, p2s2, and p4s6 was 0.72, 0.6, and 0.5 μm (Table 2). The data shown in Figure 17 indicate the following:

1. For low laser powers (cases p2s1 and p2s2), the PDAS obtained with the fluid dynamics model (HTS_FD) is larger than that with the simple HTS model.
2. For p2s1, PDAS with the fluid flow model is larger by more than 35% as compared with the PDAS obtained with the HTS model.
3. For p2s2, PDAS with the fluid flow model is larger by more than 30% as compared with the PDAS obtained with the HTS model.
4. For p4s6, PDAS exhibit similar values with and without the fluid flow as G and V did not exhibit significant variation with the fluid flow.

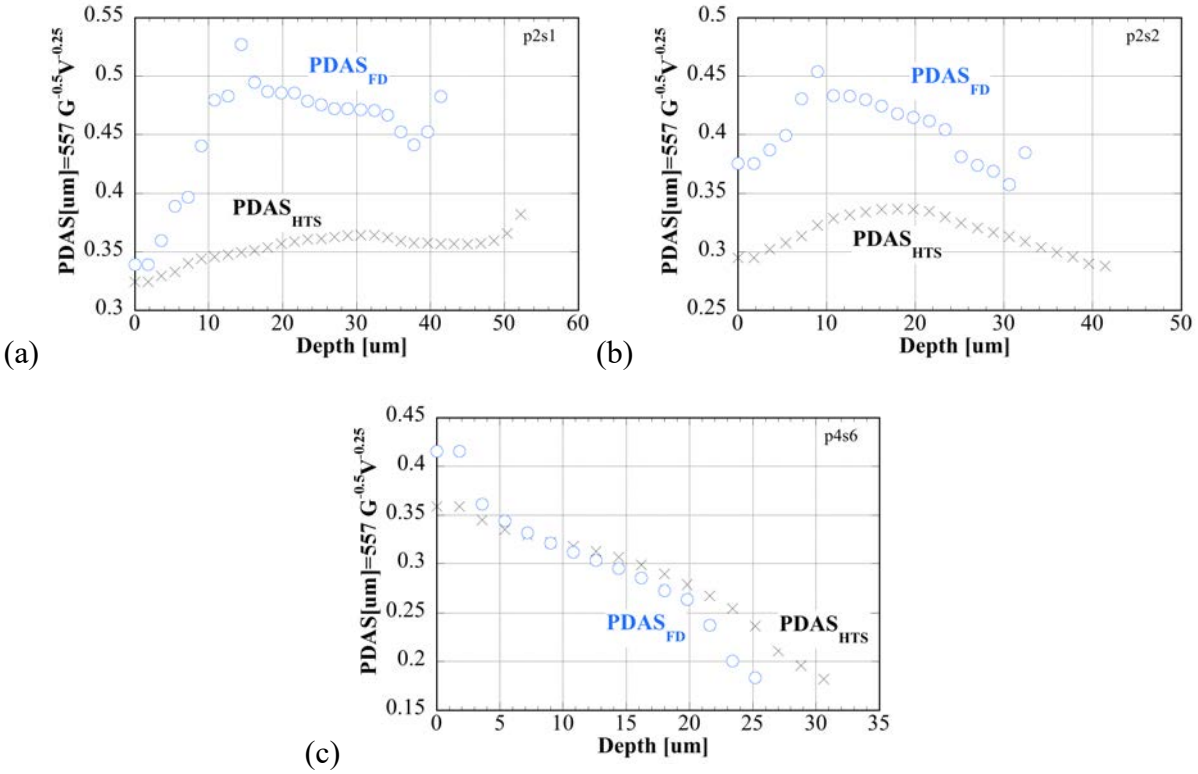

Figure 17. Distribution of PDAS, $\lambda_1[\mu m] = 557\ G[K/m]^{-0.5}\ V[m/s]^{-0.25}$, for: (a) p2s1, (b) p2s1, and (c) p4s6.

3.8 EXPERIMENTAL DATA FOR SINGLE-TRACK LASER FUSION

In order to understand the processing envelope of the laser fusion process, a wide range for laser power and laser scan speed must be investigated. Montgomery et al. (2015) considered power levels from 50 to 200 W and laser speeds from 0.2 to 1.2 m/s. In order to cover the entire processing space, 36 cases were considered, six power levels and six laser speeds over the ranges considered. At high power and low speeds, i.e., in the upper right corner of (P, U), the melt-pool is in the keyhole regime and those cases were excluded from the sensitivity study (Montgomery et al., 2015). To further assess the keyhole regime, the scaling developed in Hann et al. (2010) and King et al. (2014) for the keyhole regime based on a normalized enthalpy can be written, as:

$$\frac{P}{\sqrt{U}} > 6\frac{\pi\,\rho\,C_p T_m\sqrt{\alpha\,d_b}}{A_\lambda}. \quad (14)$$

Using IN625 thermophysical properties and for a laser beam of 80 um, the keyhole criteria becomes $\frac{P}{\sqrt{U}} > 434$ [W/ (m/s)$^{-0.5}$]

In this study, the ranges for the power and scan speeds were considered to be 50-300 W and 0.1-1 m/s, respectively. Several cases were selected at different laser powers and scanning speeds in order to cover a wide range of process parameters in order to understand the processing envelope of the laser fusion process. Cases with $\frac{P}{\sqrt{U}} > 434$ W/ (m/s)$^{-0.5}$ were indicated in Table 17 with gray cells and were excluded from evaluation in this study. Thus, in addition to the three cases introduced in previous Sections (p2s1, p2s2, and p4s6), additional six cases were considered for experimental assessment (Table 18). The SEM micrographs are shown in Figure 18.

Table 17. Calculated variable P/U$^{0.5}$ used to identify conduction-regime cases.

	Speed (m/s)					
Power (W)	**0.1**	**0.2**	**0.25**	**0.5**	**0.75**	**1**
50	158	111	100	70	57	50
75	237	167	150	106	86	75
100	316	223	200	141	115	100
150	474	335	300	212	173	150
200	632	447	400	282	230	200
250	790	559	500	353	288	250
300	948	670	600	424	346	300

Table 18. Cases considered for the STLF experimental test matrix for process map assessment in the conduction regime.

	Speed (m/s)					
Power (W)	**0.1**	**0.2**	**0.25**	**0.5**	**0.75**	**1**
50						
75	p2s1	p2s2		p2s4		p2s6
100						
150	-	p4s2		p4s4		p4s6
200	-	-				
250	-	-	-			
300	-	-	-	p7s4		p7s6

Table 19. PDAS [um] measurements for all process map cases.

	Speed (m/s)					
Power (W)	**0.1**	**0.2**	**0.25**	**0.5**	**0.75**	**1**
50						
75	0.72	0.6		0.41		0.33
100						
150	-	1.17		0.57		0.5
200	-	-				
250	-	-	-			
300	-	-	-	0.92		0.6

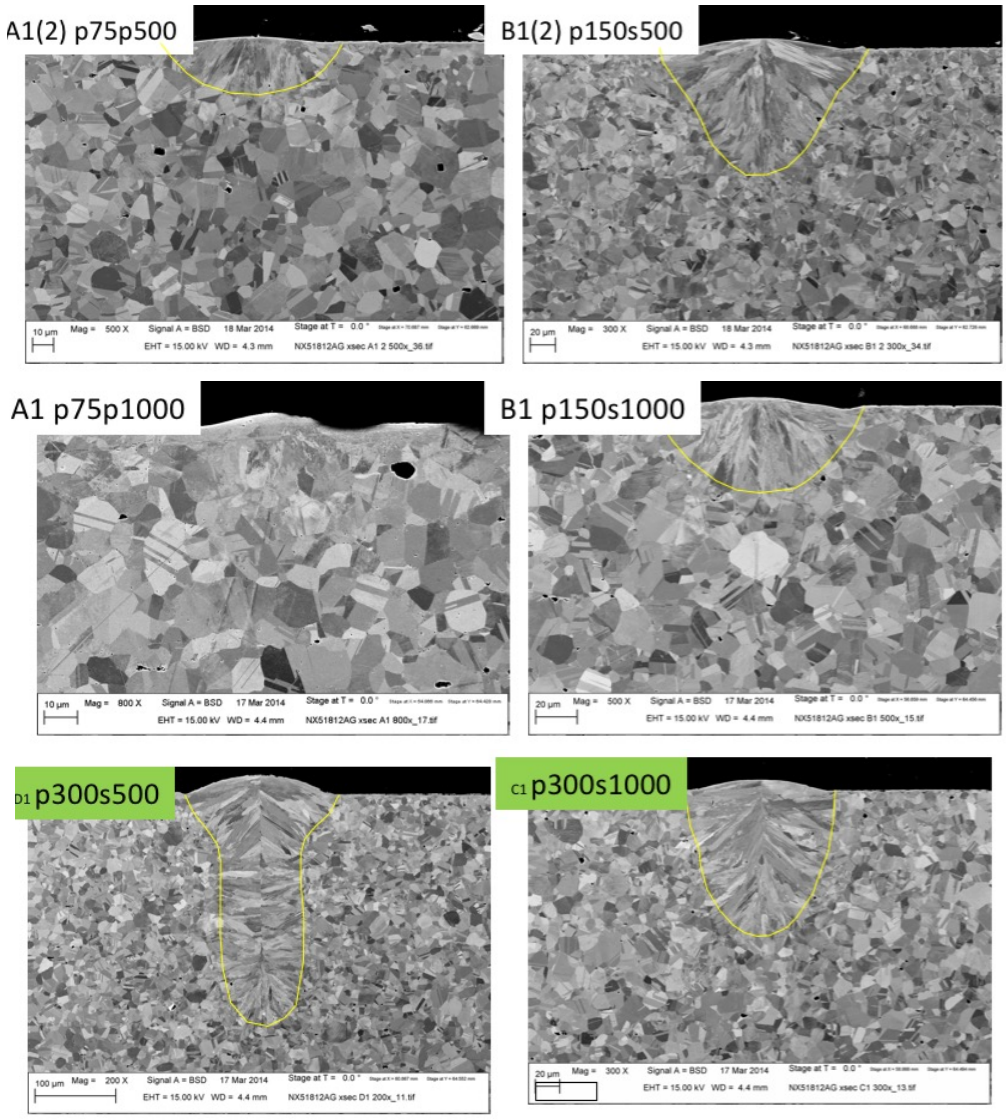

Figure 18. SEM micrographs of the melt-pool for single laser track experiments for process maps: (a) p2s4, (b) p2s6, (c) p4s2, (d) p4s4, (e) p7s4, and (f) p7s6.

3.9 ANALYSIS OF MICROSTRUCTURE RELATED VARIABLES FOR PROCESS MAPS

Thirty-three cases with different power levels and laser scan speeds were selected for conducting multi-physics STLF process simulations and to obtain microstructure-related variables to be used for developing the process maps (Table 18). The cases for which experimental data were available were marked with red font. In total, 57 simulations for the process map were considered: 33 simulations for heat-transfer-only, without fluid flow (Table 18), and 24 simulations with fluid flow (Table 19). Not all fluid flow cases converged (Figure 19). The spatial distribution of data for the microstructure-related variables, similar to those shown in Figure 11 and 12 for the G and V, were used to extract the variation along the centerline of the melt pool.

Table 20. Case ID for HTS simulations for the process maps.

	Speed (m/s)					
Power (W)	**0.1**	**0.2**	**0.25**	**0.5**	**0.75**	**1**
50	1	2	3	4	5	6
75	7	8	9	10	11	12
100	13	14	15	16	17	18
150	-	19	20	21	22	23
200	-	-	24	25	26	27
250	-	-	-	28	29	30
300	-	-	-	31	32	33

Table 21. Case ID for fluid flow (HTS_FD) simulations for the process maps.

	Speed (m/s)					
Power (W)	**0.1**	**0.2**	**0.25**	**0.5**	**0.75**	**1**
50				4	5	6
75	7	8	9	10	11	12
100			15	16	17	18
150	-	19	20	21	22	23
200	-	-	24	25	26	27
250	-	-	-	28		30
300	-	-	-	31	32	33

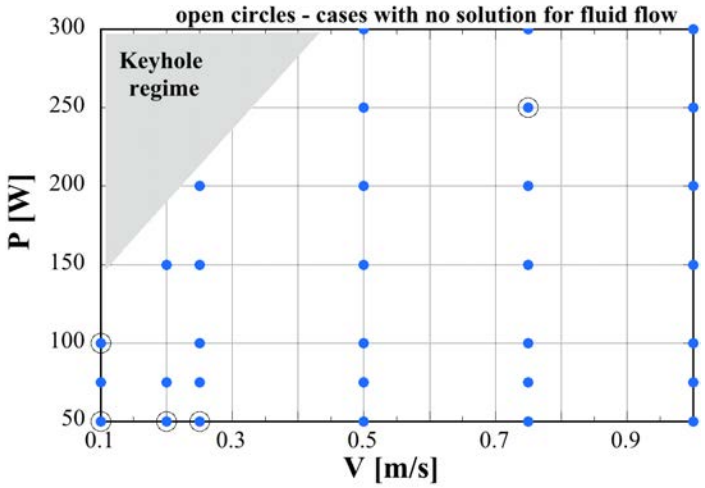

Figure 19. Cases run for the fluid flow model (HTS_FD).

3.9.1 Results for microstructure-related variables obtained for process-map cases

The variation of the solidification velocity, V, as a function of thermal gradient, G, along the centerline of the melt-pool for process map cases at constant power of 75 W is shown in Figure 20. These cases were identified as cases 7, 8, 10, and 12 for which the laser speed was 0.1, 0.2, 0.5, and 1 m/s, as shown in Table 5. Figure 20a shows the V(G) data for the heat-transfer-only simulations while Figure 20b shows the V(G) variation for the fluid flow simulations. The data shows that solidification velocity is similar in magnitude for the heat-transfer-only and fluid-flow simulations, while the thermal gradient for the fluid-flow simulations is smaller than that for the corresponding heat-transfer-only simulations.

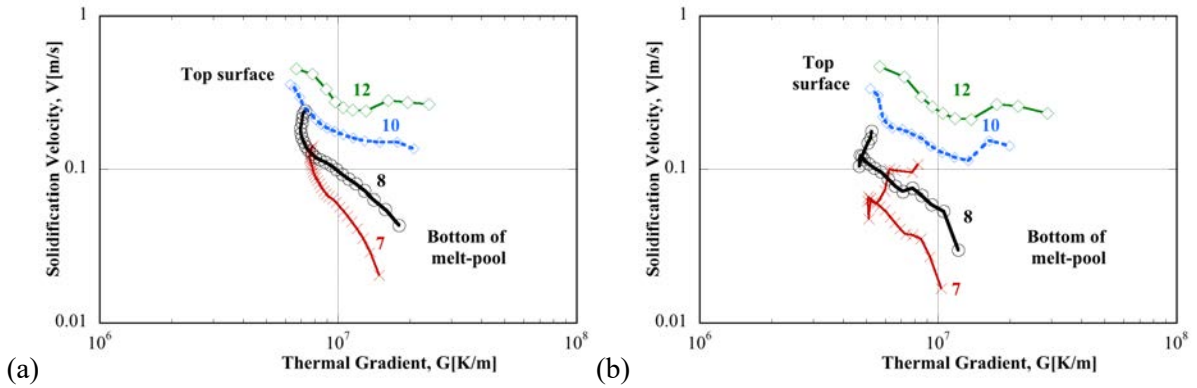

Figure 20. Solidification maps V(G) at constant power of 75 W at laser speed of 0.1, 0.2, 0.5, and 1 m/s (a) heat-transfer-only simulations, and (b) fluid flow simulations.

The solidification map along the vertical centerline of the melt-pool for all heat-transfer-only HTS cases is shown in Figure 21. It has to be mentioned that the microstructure selection map based on Hunt's model for IN625 need to be updated for the specific alloy conditions, e.g., number of nucleation sites. Thus, the solidification maps presented in this section were assembled for the sake of completion. These solidification maps can be updated as more data would be available about the microstructure selection map based on Hunt's model. Here, the data on the vertical centerline was chosen as being representative for the typical V(G) variation within the entire melt-pool. The solidification map along the vertical centerline of the melt-pool

for the fluid flow HTS_FD cases is shown in Figure 22. The data shows that that near the top-region (shown with t,c subscripts) is characterized by minimum values for G and highest values for V. On the bottom region of the melt-pool (shown with mp subscripts), maximum values for G were observed and minimum values for V, in contrast with the top-region data. The data shows that for the solidification conditions in all the cases run, a columnar dendritic microstructure is expected.

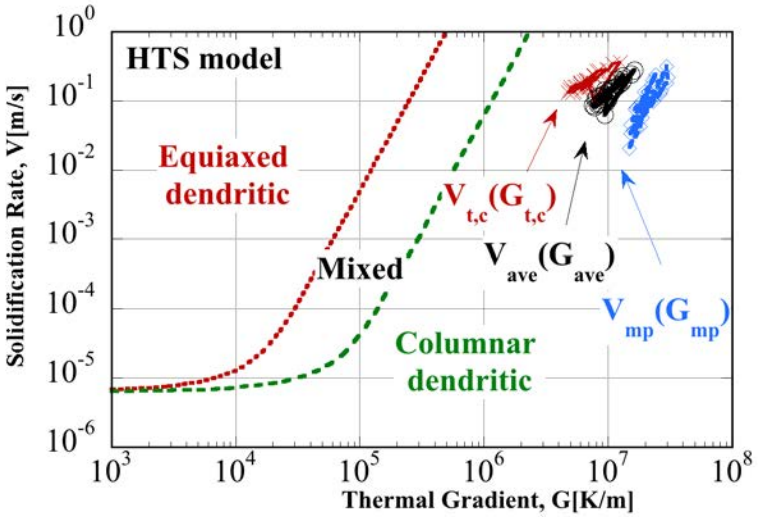

Figure 21. Solidification maps V(G) along the centerline of the melt-pool for all 33 HTS cases.

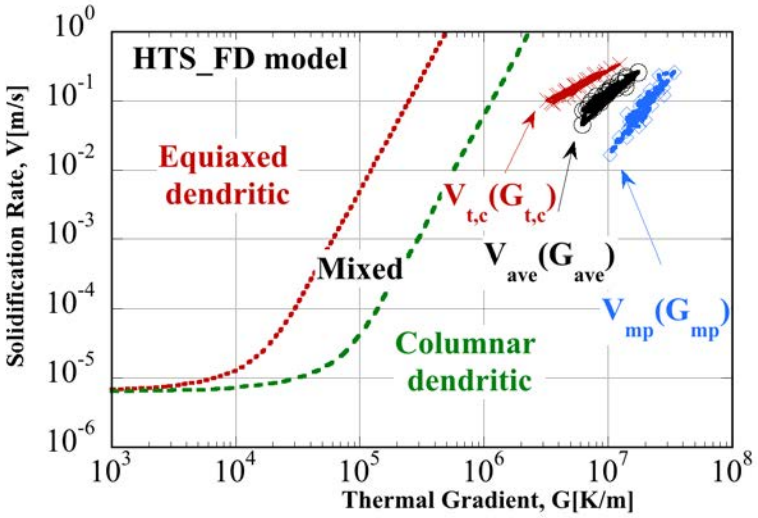

Figure 22. Solidification maps V(G) along the centerline of the melt-pool for all 24 fluid-flow HTS_FD cases.

In Figure 23, a correlation was attempted for the thermal gradient, G, as a function of a new variable, variable Power/Speed$^{0.5}$. The data shows that the thermal gradient at the top-region of the melt-pool, its average over the entire dataline, and its minimum value (at the melt-pool edge) exhibit an exponential variation with respect to $\frac{P}{\sqrt{U}}$, as:

$$G(P,U) = C_1 e^{-c_2 \frac{P}{\sqrt{U}}} \quad (15)$$

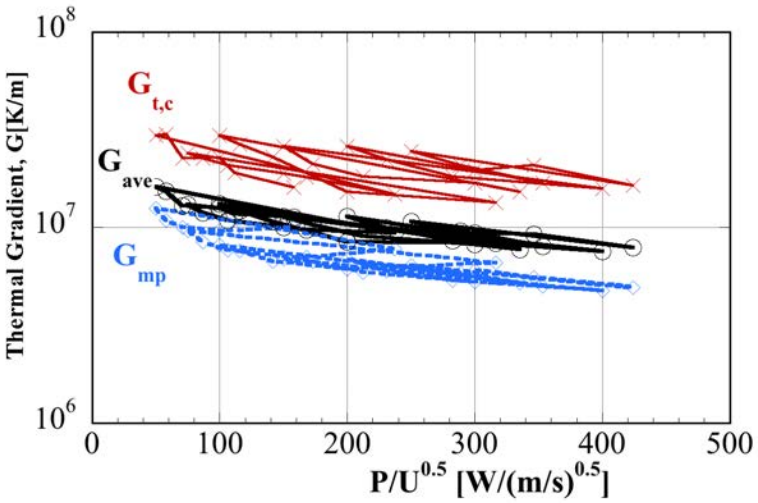

Figure 23. The variation of the thermal gradient, G, along the centerline of the melt-pool for all HTS cases as a function of the variable Power/Speed$^{0.5}$ [W/(m/s)$^{0.5}$].

4. SUBJECT INVENTIONS (AS DEFINED IN THE CRADA)

None.

5. COMMERCIALIZATION POSSIBILITIES

Commercialization possibilities will be explored at GE Global Research (GEGR). GEGR headquartered in Niskayuna, NY, is one of the world's oldest and most diverse industrial research facilities. GEGR has proven expertise and capability in Additive manufacturing (AM), with a well-established record of delivering key technological advancements through partnerships with universities, national laboratories, and industrial partners. GE is committed to the development of equipment, materials, and processes that will mature AM technology from a prototyping tool to a production process across all GE businesses. GE Global Research is equipped with total six powder-bed laser AM machines – three from SLM Solutions and three dual-beam M2 Cusing from Concept Laser, a GE Additive Company. In addition, GE Aviation, a close partner of GE Global Research, is the largest user of metal powder-bed technology in the world. 40,000 AM nozzles will be produced each year at GE's facility in Auburn, Alabama. GE also committed $32 million additive manufacturing research Centre in Findlay Township, Pennsylvania to support technical development.

6. PLANS FOR FUTURE COLLABORATION

Possible plans for future collaboration in the near future include:

1. Another phase I for HPC4Mfg program, would investigate the fluid dynamics effects on the solidification microstructure for the single-track laser fusion (STLF) conditions. Here the microstructural models for the primary dendrite arm spacing (PDAS) and solidification maps will be updated for the GERC experimental conditions in order to enable a quantitative analysis of the microstructure distribution for STLF.
2. A phase II for HPC4Mfg program. This second option extend Truchas from the current single-track laser fusion (STLF) to the full Laser Powder Bed Fusion Additive Manufacturing (LPBFAM) process. The data in phase I (this project) indicated that a comprehensive fluid flow model is needed to fully cover all the process conditions, including the keyhole regime. Thus, the Truchas's existent free-surface model, which was fully validated for pure fluid flow simulations without phase changes, will be changed to account for the recoil pressure effect and free-moving boundaries at the top surface, from what is now a fixed horizontal surface.

7. CONCLUSIONS

In this project, multi-physics simulations were conducted using a highly parallel open-source code, Truchas, with the ultimate goal of providing experimentally validated process maps for tailoring microstructure to achieve desired performance for the Laser Powder Bed Fusion Additive Manufacturing (LPBFAM) process. As a critical step towards fully LPBFAM modeling, modeling of single-track laser fusion (STLF) were conducted. The availability of the open-source code enabled the development of several user-subroutines to handle boundary conditions that were found to be crucial to the modeling of the STLF process. From numerical simulation results, several variables, such as thermal gradient, G, and solidification velocity, V, were obtained in order to predict the microstructure type (e.g., dendritic, cellular) and its length-scale. Multi-physics models considered heat transfer, phase-change, evaporation, fluid dynamics, and surface tension phenomena. In order to assess the effect of the fluid dynamics on the solidification and ensuing microstructure, a heat transfer-and-solidification-only (HTS) model and a fully coupled heat-transfer-solidification and fluid-dynamics (HTS-FD) model were considered. In the HTS_FD model, the fluid flow was considered to be laminar while the molten alloy surface is assumed to be flat and non-deformable. In all, a total of final 102 simulations were conducted at HPC systems at ORNL including Titan and CADES. The overall computational effort including all the simulations was estimated to be at approximately 1.57 MCH (million core hours).

The numerical simulation results indicate that the fluid dynamics and surface tension phenomena affect the distribution of the solidification and microstructure within the melt-pool. The results also show that the melt-pool shape is affected by the fluid dynamics. Experimental data at GEGR, provided as in-kind for this project, indicate that the liquid pool shape is elongated, similar to the predicted melt-pool for the case when the fluid dynamics and surface tension phenomena were considered.

A methodology for combining a global-master simulation and a local simulation were developed to reduce the CPU time required to simulate LPBFAM. The Truchas code was adjusted to handle the moving system of reference simulations needed for the local simulation. Since

significant resources beyond the scope of this project were needed to postprocess the steady-state results from the local simulation to obtain the microstructure variables, the full implantation of the global-local simulations was halted.

In order to validate Truchas for STLF and LPBFAM modeling, experimental data, which was obtained at GEGR for liquid pool shape and microstructure, were compared with those from numerical simulation results. The applicability of the current Truchas code to simulate a keyhole regime case was evaluated. For this keyhole regime case, numerical simulation results indicate that the melt-pool shape was typical to that of the conduction case with deviations as large as 78% from the measured melt-pool depth. Thus, only cases in the conducting regime were considered for remainder of the project. Two sensitivity studies were conducted by varying the evaporation flux and the surface tension coefficient at fixed laser absorptivities of 0.5 and 0.3, respectively. The overall combined error between the calculated values with the HTS_FD model and measured values for both width and height of the melt-pool dimensions was attained for a surface tension coefficient of -0.75e-4 N/m.

An analytical solidification model for the columnar-to-equiaxed transition (CET) in rapid solidification was used to assess the microstructure variation within the melt-pool. The solidification map CET model was developed by Hu et al. (2018) based on Hunt (1984) Gäumann et al. (2001) formalisms. Without having experimental data on the number of nucleation sites for the experiments modeled, the CET curves used in this study for IN625 were those obtained by Hu et al. (2018) at volume fraction of equiaxed dendrites of 0.66% and 49%. From numerical simulation results, thermal gradient, G, and solidification velocity, V, were obtained in order to predict the microstructure type (e.g., dendritic, cellular). The spatial distribution of the microstructure variables in a vertical cross-section through the solidified track of liquid pool, normal to the laser scanning direction, were obtained. For the fluid-flow HTS_FD model, G was found to exhibit a maximum at the extremity of the solidified pool (i.e., at the free surface). By contrast, for HTS simulations, G was found to exhibit a maximum around the entire edge of the solidified pool. For the HTS_FD simulations, the minimum values of the cooling rate, GV, were found to be approximately half than their corresponding values for HTS simulations. By contrast with the min GV values, the maximum values for GV were found to occur for the HTS_FD simulations. Thus, HTS_FD simulations were found to exhibit a wider range of cooling rates than the HTS simulations.

Concerning the solidification maps, the variation of the solidification velocity, V, as function of the thermal gradient, G, was obtained along five representative data lines. The fluid flow model results (HTS_FD) exhibited an increased spread in the V(G) variation within the melt pool with respect to the HTS model results (without the fluid flow). The fluid flow model results (HTS_FD) exhibited a decrease in the variation of solidification velocity with the thermal gradient (i.e., flatter profiles).

A correlation model based on Hunt's (1979) power law dependence on thermal gradient and solidification velocity for primary dendrite arm spacing (PDAS), which was developed by Ghosh et al. (2018) using the data on G and V from HTS simulations. Although this analytical PDAS expression is an acceptable initial correlation, this analytical expression needs to be recalibrated in the future for quantitative studies as different material properties are used in the HTS model in this study than that used by Ghosh et al. (2018) and Keller et al. (2017). For the sake of

simplicity, the PDAS recalibration was not conducted in this study and the PDAS values should be used for identifying the qualitative distribution of PDAS and not its absolute values. For low laser powers and low laser speeds, the PDAS obtained with the fluid dynamics model (HTS_FD) was larger by more than 30% with respect to the PDAS calculated with the simple HTS model.

In the second part of the project, fifty-seven simulations were conducted in order to obtain data on microstructure variables that can be used for process map development: 33 simulations with the heat-transfer-only (HTS) model and 24 simulations with the fluid flow model (HTS_FD). The solidification map data shows that for all simulations, a columnar dendritic microstructure would be expected. It was found that the minimum, average, and maximum thermal gradient exhibit exponential variations with respect to a process variable defined as the ratio between the power and square root of scan speed. The simulation data for the fluid-flow model (HTS_FD) indicated that the fluid flow and surface tension effects must be considered when developing the process map for the STLF and finally for LPBFAM process.

8. REFERENCES

Wohlers Associates, Inc., Wohlers Report 2015, 3D Printing and Additive Manuf. State of the Industry Annual Worldwide Progress Report.

Columbus, L., 2015, 2015 Roundup Of 3D Printing Market Forecasts And Estimates, http://www.forbes.com/sites/louiscolumbus/2015/03/31/2015-roundup-of-3d-printing-market-forecasts-and-estimates/

AMO - Advanced Manufacturing Office of US DOE, Additive Manufacturing: Pursuing the Promise, DOE/EE-0776, 2012, https://www1.eere.energy.gov/manufacturing/pdfs/additive_manufacturing.pdf

Huang et al., J. Clean Prod., 2015 (in Press, http://dx.doi.org/10.1016/j.jclepro.2015.04.109)

Frazier, W. Metal additive manufacturing: a review, ASM Int., 23(2014), p1917.

Bontha, el at., J Mat. Proc Tech., 178(2006), p135

Vasinonta, el at., J Manuf. Sci. Eng., 129(2007), p101

Vasinonta, A., Beuth, J. L., and Griffith, M., 2001, "A Process Map for Consistent Build Conditions in the Solid Freeform Fabrication of Thin-Walled Structures," J. Manuf. Sci. Eng., 123, pp. 615–622.

Vasinonta, A., Beuth, J. L., and Griffith, M., 1999, "Process Maps for Laser Deposition of Thin-Walled Structures," "*Solid Freeform Fabrication Proceedings*", D.L.Bourell, J.J.Beaman, R.H.Crawford, H.L.Marcus, and J.W.Barlow, eds., The University of Texas at Austin, August, pp. 383–391.

Beuth, J. L., and Klingbeil, N. W., 2001, "The Role of Process Variables in Laser-Based Direct Metal Solid Freeform Fabrication," JOM, Vol. 53, pp. 36–39.

Bikas, H., Stavropoulos, P. & Chryssolouris, G., Additive manufacturing methods and modelling approaches: a critical review, Int J Adv Manuf Technol (2016) 83: 389.

B. Schoinochoritis, D. Chantzis and K. Salonitis, Simulation of metallic powder bed additive manufacturing processes with the finite element method: A critical review, Proc IMechE Part B:J Engineering Manufacture 2017, Vol. 231(1) 96–117.

R. Glang, Vacuum Evaporation, Handbook of Thin Film Technology, Chapter 1, (editors Leon I. Maissel and Reinhard Glang) McGraw-Hill, 1970.

Hunt, Steady state columnar and equiaxed growth of dendrites and eutectic. *Materials science and engineering*, *65*, pp. 75-83 (1984).

Rappaz, M. (1989), Modelling of microstructure formation in solidification processes. *Int. Materials Reviews*, *34*(1), 93-124.

Gäumann, M., Bezencon, C., Canalis, P., and Kurz, W. (2001), Single-crystal laser deposition of superalloys: processing–microstructure maps. *Acta materialia*, *49*(6), 1051-1062.

Ghosh S., Ma L. and Ofori-Opoku N., and J.E. Guyer, On the primary spacing and microsegregation of cellular dendrites in laser deposited Ni–Nb alloys, Modelling Simul. Mater. Sci. Eng. 25 (2017) 065002 (21pp)

Kurz W and Trivedi R 1994 Rapid solidification processing and microstructure formation, Mater. Sci. Eng. A 179 46–51

Du L., Gu D., Donghua Dai, Qimin Shi, Chenglong Ma, Mujian Xia, Relation of thermal behavior and microstructure evolution during multi-track laser melting deposition of Ni-based material, Optics & Laser Technology, Vol. 108, 2018, pp. 207-217.

Kurz, W., Fisher, D.J.: Fundamentals of Solidification. Trans Tech Publications, Zurich, Switzerland (1998)

Rappaz, M., Dantzig, J.A.: Solidification. Engineering sciences. EFPL Press (2009)

Saunders, N., Guo, U. K. Z., Li, X., Miodownik, A. P., & Schillé, J. P. (2003). Using JMatPro to model materials properties and behavior. *Jom*, *55*(12), 60-65.
Raghavan, N. "Understanding Process-Structure Relationship for Site-Specific Microstructure Control in Electron Beam Powder Bed Additive Manufacturing Process Using Numerical Modeling" University of Tennessee Knoxville, 2017.
Raghavan, N., Dehoff, R., Pannala, S., Simunovic, S., Kirka, M., Turner, J., Carlson, N., Babu, S.S.: Acta Materialia 112, 303–314 (2016)
Raghavan, N., Simunovic S., Ryan Dehoff, Alex Plotkowski, John Turner, Michael Kirka, and Suresh Babu, "Localized melt-scan strategy for site specific control of grain size and primary dendrite arm spacing in electron beam additive manufacturing." *Acta Materialia* 140 (2017): 375-387.
Ghosh, S., Ma, L., Levine, L.E. et al. JOM (2018) 70: 1011. https://doi.org/10.1007/s11837-018-2771-x
Keller, T., Lindwall, G., Ghosh, S., Ma, L., Lane, B., Zhang, F., Kattner, U.R., Lass, E.A., Heigel, J.C., Idell, Y., Williams, M.E., Allen, A.J., Guyer, J.E., Levine, L.E.: Acta Materialia 139, 244–253 (2017).
Ma D and Sham P R 1998 Primary spacing in directional solidification Metall. Mater. Trans. A Vol. 29, pp. 1113–9
Bouse G K and Mihalisin J R 1989 Metallurgy of investment cast superalloy components Superalloys Supercomposites Superceramics ed J K Tien and T Caulfield (New York: Academic) p 99–148.
Hunt J D 1979 Cellular and primary dendrite spacings Proc. Int. Conf. on Solidification and Casting of Metal (London: The Metal Society) pp 3–9
Kurz W and Fisher DJ 1981 Dendrite growth at the limit of stability: tip radius and spacing, Acta Metall., Vol. 29, pp. 11–20.
Hu, Y.L., Lin, X., Lu, X.F. et al. J Mater Sci (2018), Vol. 53, pp. 15650-15666.
Nastac, L. Modeling and Simulation of Microstructure Evolution in Solidifying Alloys, Kluwer Academic Publishers, Boston/Dordrecht/London, 2004.
D.A. Korzekwa, Truchas - a multi-physics tool for casting simulation, Int. J. Cast. Met. Res. 22 (2009) 187e191.
Whitesell, H.S., Li, L. and Overfelt, R.A. Influence of solidification variables on the dendrite arm spacings of Ni-based superalloys, Metall and Materi Trans B (2000) 31: 546.
J.U Brackbill, D.B Kothe, C Zemach, A continuum method for modeling surface tension, J. Comp. Phys. 100, 335–354 (1992).
M.M. Francois, et al., J. Comp. Phys. 213, 141–73 (2006).
Francois M. M., Sicilian J. M., Kothe D. B., Modeling of Thermocapillary Forces within a Volume Tracking Algorithm, TMS Society, Modeling of Casting, Welding, and Advanced Solidification Processes, pp. 935-942, TMS, Warrendale PA, 2006.
Bell, J.B., Collela, P., and Glaz, H.M., A Second-Order Projection Method for the Incompressible Navier-Stokes Equations, Journal of Computational Physics, Vol. 85, pp. 257-283, 1989.
Bell, J.B., and Marcus, D.L., A Second-Order Projection Method for Variable-Density Flows, Journal of Computational Physics, Vol. 101, pp. 334-348, 1992.
Almgren, A.S., Bell, J.B., and Szymczak, W.G., ``A Numerical Method for the Incompressible Navier-Stokes Equations based on an Approximate Projection," SIAM J. Sci. Comput., Vol. 17, pp. 358-369, 1996.

A.V. Reddy, D.B. Kothe, C. Beckermann, R.C. Ferrell, and K.L. Lam: *Proceedings of the Fourth Decennial International Conference on Solidification Processing*, J. Beech and H. Jones, eds., The University of Sheffield, UK, 1997, pp. 83-87.

Sabau, A.S., Han, Q., and Viswanathan, S., *Projection Methods for Interdendritic Flows,* in Proceedings of Fluid Flow Phenomena in Metals Processing, TMS Annual Meeting, San Diego, February 28-March 4, 1999, pp. 403-413.

Sabau, A.S., and Viswanathan, S., *Microporosity prediction in aluminum alloy castings,* Metals and Metallurgical Transactions, B, 2002, Vol. 33B, pp. 243-255.

Saldi ZS, Marangoni driven free surface flows in liquid weld pools, PhD thesis, Delft University of Technology, ISBN 9461909802, 9789461909800, 2012.

R. Choo, J. Szekely, and S. David, "On the calculation of the free surface temperature of gas-tungsten-arc weld pools from first principles: Part ii. modeling the weld pool and comparison with experiments," Metallurgical and Materials Transactions B, vol. 23, pp. 371–384, 1992.

R. T. C. Choo and J. Szekely, "Possible role of turbulence in gta weld pool behavior," Welding Journal, vol. 73, pp. 25s–31, 1994.

C. Chan, J. Mazumder, and M. M. Chen, "A two-dimensional transient model for convection in laser melted pool," Metallurgical Transactions A - Physical Metallurgy and Materials Science, vol. 15, pp. 2175–2184, 1984.

C. L. Chan, J. Mazumder, and M. M. Chen, "3-dimensional axisymmetrical model for convection in laser melted pools," Materials Science and Technology, vol. 3, pp. 306–311, 1987.

C. Chan, J. Mazumder, and M. M. Chen, "A three-dimensional model for convection in laser melted pool," Journal of Metals, vol. 35, no. 12, p. 47, 1983.

K. Mundra and T. DebRoy, "Toward understanding alloying element vaporization during laser beam welding of stainless steel," Welding Journal, vol. 72, no. 1, pp. 1–9, 1993.

B. Ribic, R. Rai, and T. DebRoy, "Numerical simulation of heat transfer and fluid flow in GTA/laser hybrid welding," Science and Technology of Welding and Joining, vol. 13, no. 8, pp. 683–693, 2008.

W. Pitscheneder, T. DebRoy, K.Mundra, and R. Ebner, "Role of sulfur and processing variables on the temporal evolution of weld pool geometry during multikilowatt laser beam welding of steels," Supplement to the Welding Journal, p. 71s, 1996.

E. J. Ha and W. S. Kim, "A study of low-power density laser welding process with evolution of free surface," International Journal of Heat and Fluid Flow, vol. 26, no. 4, pp. 613–621, 2005.

R. T. C. Choo and J. Szekely, "Possible role of turbulence in GTA weld pool behavior," Welding Journal, vol. 73, no. 2, pp. 25–31, 1994.

K. Hong, D. C. Weckman, A. B. Strong, and W. Zheng, "Modelling turbulent thermofluid flow in stationary gas tungsten arc weld pools," Science and Technology of Welding and Joining, vol. 7, no. 3, pp. 125–136, 2002.

K. Hong, D. C. Weckman, A. B. Strong, and W. Zheng, "Vorticity based turbulence model for thermofluids modelling of welds," Science and Technology of Welding and Joining, vol. 8, no. 5, pp. 313–324, 2003.

Bauer H.F., Eidel W., Thermo-capillary convection in various infinite rectangular container configurations, Heat and Mass Transfer, Vol. 40, pp. 123-132, 2003.

Y.P. Lei, Hidekazu Murakawa, Y.W. Shi, X.Y. Li, Numerical analysis of the competitive influence of Marangoni flow and evaporation on heat surface temperature and molten

pool shape in laser surface remelting, Computational Materials Science, Vol. 21, pp. 276-290, 2001.
Saunders, N., Guo, U. K. Z., Li, X., Miodownik, A. P., & Schillé, J. P. Using JMatPro to model materials properties and behavior. *JOM*, *55*, pp. 60-65. 2003.
Compton, E. C., "Evaluation of a Standard Test Method for Total Hemispherical Emittance of Surfaces from 293 K to 1673 K," NASA TM-87681, NASA Langley Research Center (January 1986).
S. Boyden and Y. Zhang, "Temperature and Wavelength-Dependent Spectral Absorptivities of Metallic Materials in the Infrared", Journal of Thermophysics and Heat Transfer, Vol. 20, (2006), pp. 9-15.
Chen, J. and Ge, XS, An Improvement on the Prediction of Optical Constants and Radiative Properties by Introducing an Expression for the Damping Frequency in Drude Model, International Journal of Thermophysics (2000) 21: 269.
Bramson, M. A., 1968, Infrared Radiation: A Handbook for Applications (Plenum, New York).
DebRoy T. and David S. A., Physical processes in fusion welding. Rev. Mod. Phys., Vol. 67, pp. 85–112 (1995).
Matsushita T, Fecht H-Jr, Wunderlich RK, Egry I, Seetharaman S. Studies of the Thermophysical Properties of Commercial CMSX-4 Alloy. J Chem Eng Data. 2011;54(9):2584-92.
JJ. Valencia and P.N. Quested, ASM Handbook, Volume 15: Casting, Thermophysical Properties, DOI: 10.1361/asmhba0005240, 2008, pp. 468-481.
Aune, R. E., Battezzati, L., Brooks, R., Egry, I., Fecht, H.-J., Garandet, J.-P., … Wunderlich, R. K. Thermophysical properties of IN738lc, MM247lc and CMSX-4 in the liquid and high temperature solid phase. In Superalloys 718, 625, 706 and Derivatives, Proceedings, 2005, pp. 467–476.
K. C. Mills, Y. Youssef, Z. Li and Y. Su: ISIJ Int., 2006, 46, 623–632.
I. Yadroitsev, I. Smurov, Selective laser melting technology: From the single laser melted track stability to 3D parts of complex shape, Physics Procedia, Vol. 5, Part B, 2010, pp. 551-560.
DB Hann, J Iammi, and J Folkes, A simple methodology for predicting laser-weld properties from material and laser parameters, Journal of Physics D: Applied Physics, Vol. 44, 2011.
Hann D., Iammi J., Folkes J. (2010) Keyholing or Conduction – Prediction of Laser Penetration Depth. In: Hinduja S., Li L. (eds) Proceedings of the 36th International MATADOR Conference. Springer, London.
W.E. King, Holly D. Barth, Victor M. Castillo, Gilbert F. Gallegos, John W. Gibbs, Douglas E. Hahn, Chandrika Kamath, Alexander M. Rubenchik, Observation of keyhole-mode laser melting in laser powder-bed fusion additive manufacturing, Journal of Materials Processing Technology, Vol. 214, pp. 2915-2925, 2014.
C. Montgomery, J. Beuth, L. Sheridan, and N. Klinbeil, “Process mapping of Inconel 625 in laser powder bed additive manufacturing,” Solid Freeform Fabrication Symposium Proceedings, pp. 1195–1204, 2015.

9. APPENDIX A. MATERIALS PROPERTIES

The calculated data using JMatPro software (Saunders et al., 2003) for specific heat and thermal conductivity is shown in Figure 25. Where available, the property data was compared against independent property data. For example, the calculated liquid viscosity was shown in Figure 26 against the data obtained with a formula from Mills et al. (2006), indicating a good agreement between the two sets of data. The calculated data on the surface tension coefficient is shown in Figure 27a. The surface tension coefficient, $d\sigma/dT$, was calculated as the first derivative of the data in Figure 27a and it is shown in Figure 27b.

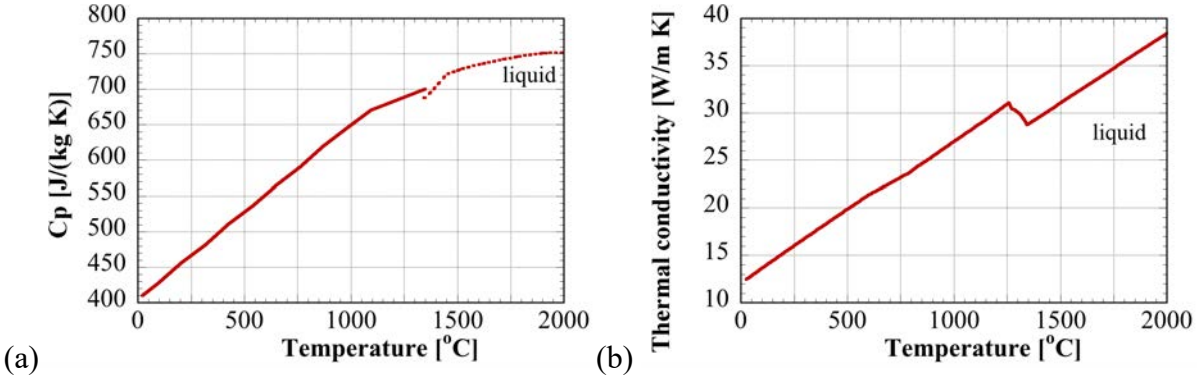

(a) (b)

Figure 24. Calculated specific heat and thermal conductivity of IN625.

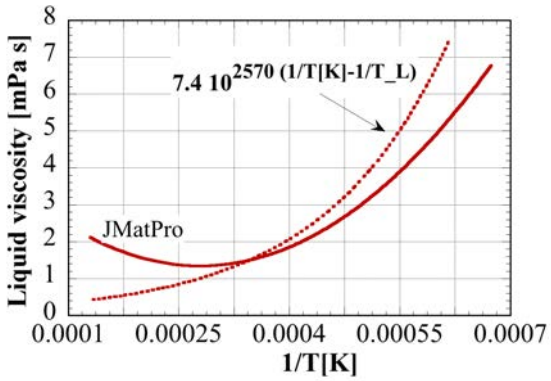

Figure 25. Calculated liquid viscosity of IN625.

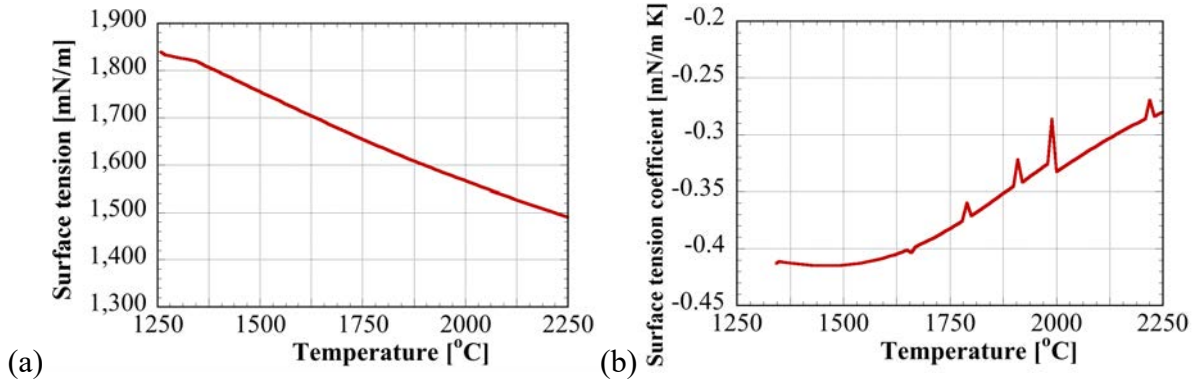

(a) (b)

Figure 26. Calculated surface tension and surface tension coefficient for IN625.

10. APPENDIX B. CUBIT MESH – JOURNAL FILE

```
brick x 1.1 y 0.5 z 0.4. ! dimensions in mm
move volume 1 x 0.55 y 0.25 z -0.2
brick x 1.1 y 0.5 z 0.6
move volume 2 x 0.55 y 0.25 z -0.7
imprint body all
merge body all
curve 4 interval 10. # X
curve 3 interval 7  # Y
curve 9 interval 8 # Z
mesh volume 1
# refine about 0.5 in the Z direction with 41.6 um
refine node in curve 4 with x_coord < 0.5 depth 4
# refine about 0.208 um in the Z direction with 13.9 um
refine node in curve 4 with x_coord < 0.6 depth 6
refine node in curve 4 with x_coord < 0.56 depth 13
curve 21 interval 6
curve 21 scheme bias factor 1.14 start vertex 7
propagate curve bias volume 2
volume 2 scheme sweep source surface 2 target surface 8
mesh volume 2
#Specify sidesets for Boundary Conditions in Truchas
# top surface
sideset 1 surface 1
# bottom surface
sideset 2 surface 8
# y min
sideset 3 surface 3 9
# x min
sideset 4 surface 4 10
# y Max
sideset 5 surface 5 11
# x Max
sideset 6 surface 6 12
# only one body
block 1 volume 1 2
block 1 element type HEX
nodeset 100 volume all
set large exodus file off
export mesh "refined_mesh_ge.exo" 1 overwrite
```

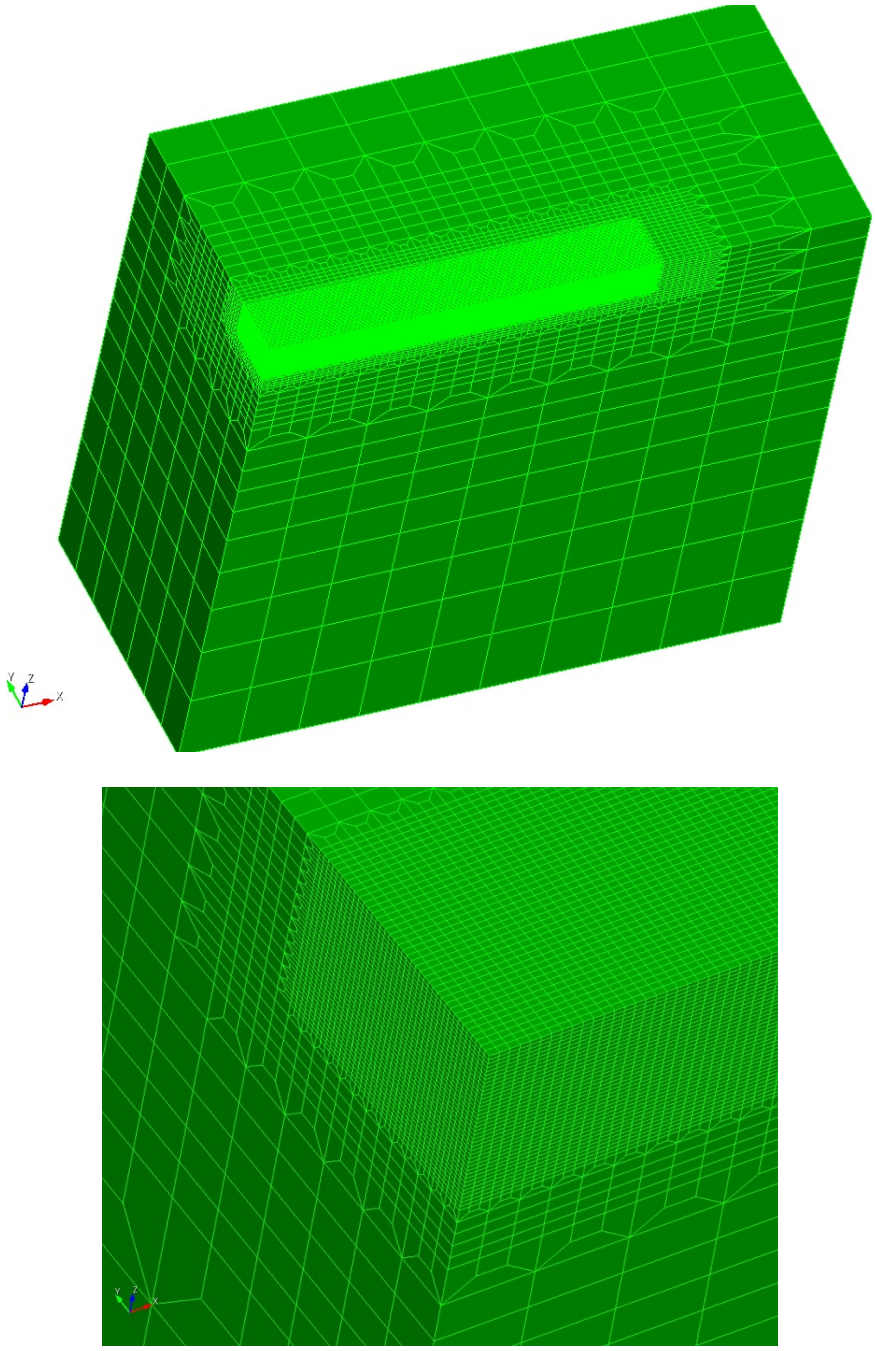

Figure 27. Pictures of the mesh: (a) entire volume and (b) close view of refined region.

11. APPENDIX C. SIMULATION SETUP

Preliminary STLF simulation runs indicated that Truchas exhibited poor convergence with the default setup for the onset of fluid flow and surface tension. The following solutions were found to overcome this poor convergence due to the early onset of the fluid flow with surface tension forces in Truchas: (1) turn on the CFD model when an adequate number of computational cells are in the liquid state, (2) restart a new CFD simulation after heat transfer and solidification simulation reached a stated state with an adequate number of fluid cells. The second option, in which the fluid dynamics simulations were conducted as a restart simulation run, is illustrated in Figure 28. The heat-transfer-and-solidification model (HTS) was run until the laser beam was scanned over a distance that is approximately three beam diameters (3 d_b). At that time, a physical time t_1=3 d_b/U would be reached, and the multi-physics heat transfer, phase-change, fluid dynamics, and surface tension (HTS_FD) simulation would be restarted. The end of the physical simulation time was selected to be t_{end}=13 d_b/U. This end-time was selected to allow enough physical simulation time to obtain the microstructure related variables within the steady state, which was estimated to be reach at a physical time of approximately 7 d_b/U. Length-scales and corresponding time-scales for the multi-simulation runs were shown in Table .

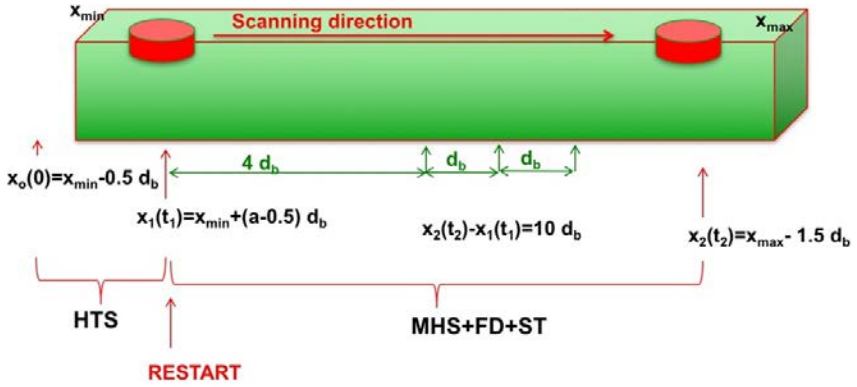

Figure 28. Schematic of combined HTS and HTS_FD simulation setup.

Table 22. Length-scales and corresponding time-scales for the HTS and HTS_FD simulation setup.

Time	Laser-beam Position	Model	Speed
0	-0.5 d_b	HTS	U
t_1	2.5 d_b	HTS	U
t_1	2.5 d_b	HTS_FD	U
t_{end}	12.5 d_b	HTS_FD	U
t_{end}	12.5 d_b	HTS_FD	0

12. APPENDIX D. TRUCHAS INPUT FILE

```
#short_remarks surface heating for laser; microstructure
#P1 (100 W), S1 (300 mm/s); Bulk alloy (Plate); M - microstructure, ST - surface
tension, E - evaporation Hertz-Knudsen for mass evaporation with Clausius-Clapeyron
for saturation pressure; Conversion factors MKS to mm,g,ms: 1 J [kg m^2 / s^2]=1e3 g
mm^2/ms^2; 1 W [J/s]=1[g mm^2 /ms^3]; 1 W/m^2 = 1e-6 [g /ms^3]

&MESH
       Mesh_File                = 'redefined_v3.exo'   ! x =0.12cm   y = 0.05cm   z =
0.1cm
/

&OUTPUTS
       Output_T                    = 0.0, 9.0
       Output_Dt                   = 0.55
       Short_Output_Dt_Multiplier  = 1
/
&DS_BOUNDARY_CONDITION
        Name                        = 'laser_beam'
        Variable                    = 'temperature'
        Condition                   = 'flux'
        Face_Set_IDs                = 1
        Data_Function               = 'moving-source'
/
&FUNCTION
        Name                        = 'moving-source'
        Type                        = 'library'
        Library_Path                = '/truchas_user_sub_ge1/libpath.so'
        Library_Symbol              = 'flux_surface_gaussian'
        Parameters                  = 0.05 0.3 75.0 0.08 3.36 0.0 10E25       ! speed,
efficiency, beam_power, beam_dia, r_max_restriction, z_top, q_max
/
&PHYSICS
  Heat_Transport             = .true.
  Fluid_Flow                 = .true.
  !Inviscid                   = .false.
  Surface_tension            = .true.
  Porous_flow     = .false. ! .true.,
  body_force = 0.0, 0.0, -9.8e-3
/
&PHYSICAL_CONSTANTS
        Stefan_Boltzmann           = 5.67e-14     ! g-mm-ms units
/
&SURFACE_TENSION
        Csf_Boundary               = .true.
        Bndry_Face_Set_Ids         = 1
        Dsig_Dt                    = -0.075e-6      ! [(g-mm/ms^2)/(mm-K)]
        Sigma_Constant             = 1.0          ! not used, but needed at input
/
&DS_BOUNDARY_CONDITION
       Name          = 'top_rad'
       Variable      = 'temperature'
       Condition     = 'radiation'
       Face_Set_IDs  = 1
       Data_Constant = 0.7, 300.0      ! Emissivity, Ambient_Temp.(K) for radiation BC
/
&DS_BOUNDARY_CONDITION
  Name          = 'top_convec'
  Variable      = 'temperature'
  Condition     = 'HTC'
```

```
  Face_Set_IDs  = 1
  Data_Constant = 15.0E-6, 300.0
/
&EVAPORATION

 face_set_ids = 1 ! identical to 'top_rad'
 prefactor = 3.378652e+09 ! A in problem units [energy/area-time
 temp_exponent = -0.5 ! beta
 activation_energy = 372100.0 ! E_a in J/mol, NOT problem units
/
&DS_BOUNDARY_CONDITION
       Name          = 'bottom'
       Variable      = 'temperature'
       Condition     = 'HTC'
       Face_Set_IDs  = 2
       Data_Constant = 1000.0E-6, 300.0     ! Initial_Temp.(K) of the bottom of the
start plate
/
&DS_BOUNDARY_CONDITION
       Name          = 'ymin'
       Variable      = 'temperature'
       Condition     = 'flux'
       Face_Set_IDs  = 3
       Data_Constant = 0.0                   ! Zero_Flux (Adiabatic BC); symmetry on
front surface
/
&DS_BOUNDARY_CONDITION
       Name          = 'xmin'
       Variable      = 'temperature'
       Condition     = 'HTC'
       Face_set_ids  = 4
       Data_Constant =  200.0E-6, 300.0                  ! htc on left surface
/
&DS_BOUNDARY_CONDITION
       Name          = 'ymax'
       Variable      = 'temperature'
       Condition     = 'HTC'
       Face_Set_IDs  = 5
       Data_Constant =  200.0E-6, 300.0                  ! htc on back surface
/
&DS_BOUNDARY_CONDITION
       Name          = 'xmax'
       Variable      = 'temperature'
       Condition     = 'HTC'
       Face_Set_IDs  = 6
       Data_Constant =  200.0E-6, 300.0                  ! htc on right surface
/
##### ASSIGN MATERIALS AND INITIAL CONDITIONS ###################

&BODY
  surface_name = 'from mesh file'
  mesh_material_number = 1
  material_number = 1
  temperature = 300.0
/
&MICROSTRUCTURE
   material = "IN625"
   cell_set_ids = 1
   ! symmetry_face_sets = 1
   grad_abs_tol = 0.0
   grad_rel_tol = 1.0e-5
   vel_max = 100.0
   vel_lo_solid_frac = 0.05
   vel_hi_solid_frac = 0.95
   gv_model_file = 'in625-gv-model1.txt'
```

```
 /
&MATERIAL
  material_name = 'IN625-sol'
  material_number = 1
  immobile= .true.
  priority = 1
  density = 1.0 ! not void
  material_feature = 'background'
/
&PHASE
 name = 'IN625-sol'
 property_name(1) = 'density',       property_constant(1) = 7.7e-3 ! g/mm^3
 property_name(2) = 'specific heat', property_function(2) = 'IN625-sol-Cp'
 property_name(3) = 'conductivity',  property_function(3) = 'IN625-sol-k'
/
&FUNCTION ! (g-mm^2/ms^2)/g-K
  name = 'IN625-sol-Cp'
  type = 'polynomial'
  poly_coefficients   = 361.8513, 0.1251116, 1.740843e-4, -7.527126e-8
  poly_exponents(1,:) = 0,        1,         2,        3
  poly_refvars(1) = 0.0  ! curve fit data in [K] not Celsius
/
&FUNCTION ! (g-mm^2/ms^3)/mm-K
  name = 'IN625-sol-k'
  type = 'polynomial'
  poly_coefficients   = 4.929465e-3, 1.574994e-5
  poly_exponents(1,:) = 0, 1
  poly_refvars(1) = 0.0  ! curve fit data in [K] not Celsius
/
&MATERIAL
  material_name = 'IN625-liq'
  material_number = 2
  immobile= .false.
  priority = 2
  density = 1.0 ! not void
/
&PHASE
  name = 'IN625-liq'
  property_name(1) = 'density',       property_constant(1) = 7.7e-3   ! g/mm^3
  property_name(2) = 'specific heat', property_constant(2) = 700.0    ! (g-
mm^2/ms^2)/g-K
  property_name(3) = 'conductivity',  property_constant(3) = 30.0e-3   ! 1 W/m-K  =  1
(kg-m/s3-K) = 10e-3 (g-mm/ms3-K)
  property_name(4) = 'viscosity',     property_function(4) = 'IN625-visc-ornl'
  property_name(5) = 'density deviation', property_function(5) = 'IN625-liq-drho'
/
&FUNCTION
  name = 'IN625-liq-drho'
  type = 'polynomial'
  poly_coefficients = 0.13567, -9.0197e-5, -7.9917e-9
  poly_exponents(1,:) = 0, 1, 2
  poly_refvars(1) = 273.0
/
&FUNCTION ! [g/mm-ms]
  name = 'IN625-visc-ornl'
  type = 'polynomial'
  poly_coefficients = -0.7891836e-6, 1.323343e-2, -4.364599e+1, 7.061531e+4
  poly_exponents(1,:) = 0, -1, -2, -3
  poly_refvars(1) = 0.0 ! curve fit data in [K] not Celsius
/
&MATERIAL_SYSTEM
  name = 'IN625'
  phases = 'IN625-sol', 'IN625-liq'
  transition_temps_low  = 1563.0  ! [K]
  transition_temps_high = 1623.0  ! [K]
```

```
  smoothing_radius = 5 ! [K]
  latent_heat = 290000.0 ! [g-mm^2/ms^2/g]
/
&DIFFUSION_SOLVER
       Abs_Temp_Tol            = 0.0
       Rel_Temp_Tol            = 1.0e-2  ! 8.0e-5  ! started with 1.0e-3
       Abs_Enthalpy_Tol        = 0.0
       Rel_Enthalpy_Tol        = 1.0e-2
       NLK_Tol                 = 0.02
       NLK_Preconditioner      = 'HYPRE_AMG'
       Max_NLK_itr             = 5
        Stepping_Method         = 'Adaptive BDF2'
        pc_amg_cycles           = 2  ! 2
        verbose_stepping        = .true.

/
&NUMERICS
       Dt_Init                 = 1.0e-05
       Dt_Max                  = 1.0e-3
       Dt_Min                  = 1.0e-14
  Courant_Number          = 0.3
  Discrete_Ops_Type       = 'ortho'
  Projection_Linear_Solution = 'projection'
  Viscous_Implicitness    = 0.5
  Viscous_Linear_Solution = 'viscous'
/
&LINEAR_SOLVER
  Name                    = 'projection'
  Method                  = 'fgmres'
  Preconditioning_Method  = 'ssor'
  Convergence_Criterion   = 1.0e-10
  Relaxation_Parameter    = 1.4
  Preconditioning_Steps   = 2
  Stopping_Criterion      = '||r||'
  Maximum_Iterations      = 2000
/
&LINEAR_SOLVER
  Name                   = 'viscous'
  Method                 = 'fgmres'
  Preconditioning_Method = 'diagonal'
  Stopping_Criterion     = '||r||/||b||'
  Convergence_criterion  = 1.0e-10
  Relaxation_Parameter   =1.0
  Preconditioning_Steps  = 5
  Maximum_Iterations     = 500
/
&PROBE
         Probe_Name = 'A_t' Probe_Coords = 0.52, 0.0, 0.0,
/
&PROBE
         Probe_Name = 'A_m' Probe_Coords = 0.52, 0.0, -0.02,
/
&PROBE
         Probe_Name = 'A_b' Probe_Coords = 0.52, 0.0, -0.04,
/
&PROBE
         Probe_Name = 'B_t' Probe_Coords = 0.6, 0.0, 0.0,
/
&PROBE
         Probe_Name = 'B_m' Probe_Coords = 0.6, 0.0, -0.02,
/
&PROBE
         Probe_Name = 'B_b' Probe_Coords = 0.6, 0.0, -0.04,
/
&PROBE
```

```
        Probe_Name = 'C_t' Probe_Coords = 0.68, 0.0, 0.0,
/
&PROBE
        Probe_Name = 'C_m' Probe_Coords = 0.68, 0.0, -0.02,
/
&PROBE
        Probe_Name = 'C_b' Probe_Coords = 0.68, 0.0, -0.04,
/
```

in625-gv-model1.txt file

```
{
  "gv-model-type": "gv1",
  "theta1": 0.05, "theta1p": 0.04,
  "theta2": 0.95, "theta2p": 0.94,

            "theta-gv": 0.10,  //  GV taken at this solid fraction
      "liquidus-slope": -7.5,  //  [K/C]
         "solute-conc": 0.50,  //  [C]
      "partition-coef": 0.61,  //  [unitless]
     "liq-sol-delta-T": 15.0,   //  [T]
         "diffusivity": 9.0e-9, //  [L^2/T]
  "gibbs-thomson-coef": 1.0e-7,  //  [K-L]
    "instability-coef": 0.1,   //  [unitless]
     "coarsening-coef": 10.0e-6    //  [L/T^{1/2}] to be updated later
}

// K = temperature unit
// L = length unit
// C = concentration unit
// T = time unit
```